



## **The Art of Constructing Black Phosphorus Nanosheet Based Heterostructures: From 2D to 3D**

Downloaded from: <https://research.chalmers.se>, 2025-12-04 16:18 UTC

Citation for the original published paper (version of record):

Thurakkal, S., Feldstein, D., Perea Causin, R. et al (2021). The Art of Constructing Black Phosphorus Nanosheet Based Heterostructures: From 2D to 3D. *Advanced Materials*, 33(3).  
<http://dx.doi.org/10.1002/adma.202005254>

N.B. When citing this work, cite the original published paper.

# The Art of Constructing Black Phosphorus Nanosheet Based Heterostructures: From 2D to 3D

Shameel Thurakkal, David Feldstein, Raúl Perea-Causín, Ermin Malic, and Xiaoyan Zhang\*

Assembling different kinds of 2D nanosheets into heterostructures presents a promising way of designing novel artificial materials with new and improved functionalities by combining the unique properties of each component. In the past few years, black phosphorus nanosheets (BPNSs) have been recognized as a highly feasible 2D material with outstanding electronic properties, a tunable bandgap, and strong in-plane anisotropy, highlighting their suitability as a material for constructing heterostructures. In this study, recent progress in the construction of BPNS-based heterostructures ranging from 2D hybrid structures to 3D networks is discussed, emphasizing the different types of interactions (covalent or noncovalent) between individual layers. The preparation methods, optical and electronic properties, and various applications of these heterostructures—including electronic and optoelectronic devices, energy storage devices, photocatalysis and electrocatalysis, and biological applications—are discussed. Finally, critical challenges and prospective research aspects in BPNS-based heterostructures are also highlighted.

## 1. Introduction


Heterostructures of layer-by-layer-assembled 2D nanosheets are an important class of materials, as these possess novel hybrid physicochemical properties and promising applications in a range of technological areas, such as nanodevices, energy conversion and storage, nanomedicines, and catalysis.<sup>[1–8]</sup> Heterostructures combine the unique intrinsic properties of different 2D materials into new hybrid materials.<sup>[9,10]</sup> In general, heterostructures are constructed by assembling different nanomaterials via covalent bond formation or noncovalent interactions using various approaches, including layer-by-layer mechanical

transfer,<sup>[11–14]</sup> chemical vapor deposition (CVD),<sup>[15–22]</sup> solvothermal processes,<sup>[23–27]</sup> and wet chemical reactions.<sup>[28]</sup> In covalently formed heterostructures, different nanomaterials are attached through direct bond formation or by bonding using organic linkers. By contrast, different nanomaterials are stacked layer-by-layer via van der Waals interactions or electrostatic interactions to form noncovalent heterostructures. A range of heterostructures has been developed by assembling various 2D materials, including graphene,<sup>[2,29]</sup> transition metal dichalcogenides (TMDs),<sup>[30–32]</sup> graphitic carbon nitride (g-C<sub>3</sub>N<sub>4</sub>),<sup>[33,34]</sup> hexagonal boron nitride (h-BN),<sup>[35,36]</sup> and transition metal carbides or nitrides (MXene).<sup>[37]</sup>

Black phosphorus nanosheets (BPNSs) are a rising star among 2D materials beyond graphene because of their unique physicochemical properties.<sup>[38–47]</sup> In black phosphorus (BP) crystals, different BP layers are stacked together via weak van der Waals interactions, and the phosphorus atoms are chemically linked to each other via sp<sup>3</sup>-hybridized covalent bonds within a layer, leaving a lone pair of electrons on each phosphorus atom.<sup>[48]</sup> BPNSs show a repeating puckered honeycomb structure along the armchair direction and a bilayer arrangement along the zigzag direction, resulting in strong in-plane anisotropic electronic and optical properties in BPNSs.<sup>[49–51]</sup> BPNSs show a wide range of thickness-dependent direct bandgaps from 0.3 eV (bulk BP) to 2.0 eV (monolayer). Their optical response is dominated by excitons, exhibiting binding energies in the range of a few hundred meV.<sup>[52,53]</sup> Furthermore, monolayer BP possesses a charge carrier mobility of 1000 cm<sup>2</sup> V<sup>−1</sup> s<sup>−1</sup> and an excellent on/off ratio of 10<sup>3</sup>–10<sup>4</sup> in field effect transistors.<sup>[54]</sup> Owing to these exciting properties, BPNSs have shown potential applications in photocatalysis, biomedicines, energy storage and conversion, and electronic and optoelectronic devices.<sup>[55–61]</sup> However, the poor stability of BPNSs under ambient conditions limits their real applications, mainly because of the chemical degradation of phosphorus atoms into phosphorus oxides in the presence of oxygen and/or water.<sup>[62–66]</sup> So far, different approaches such as chemical functionalization<sup>[67–72]</sup> and metal oxide or ionophore protective layer coating<sup>[73–75]</sup> have been demonstrated as effective methods for improving the ambient stability of BPNSs. Among the different passivation strategies, building heterostructures via covalent or noncovalent approaches (Scheme 1) can help obtain BPNS-based heterostructures with various architectures and functionalities. BPNS-based heterostructures can provide the large area passivation of BPNSs, combine the properties

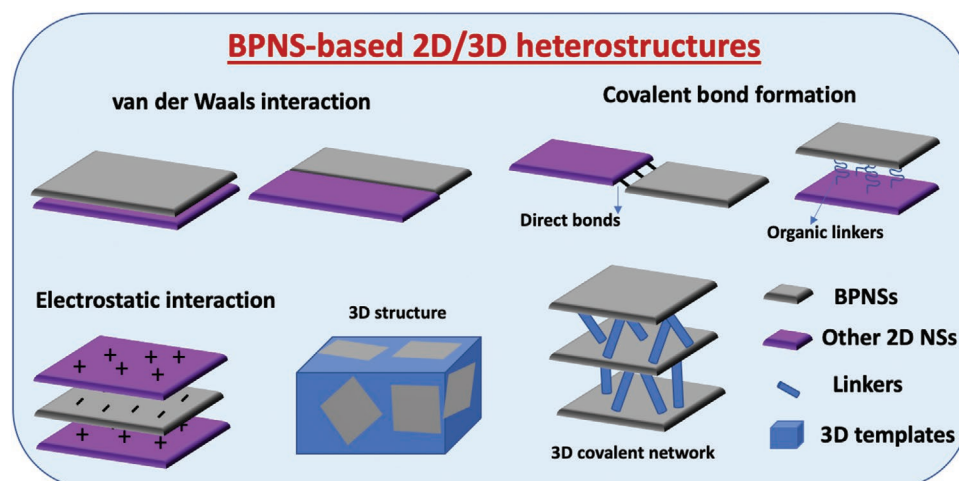
Dr. S. Thurakkal, Prof. X. Zhang  
Division of Chemistry and Biochemistry  
Department of Chemistry and Chemical Engineering  
Chalmers University of Technology  
Kemigården 4, Göteborg SE-412 96, Sweden  
E-mail: xiaoyan.zhang@chalmers.se

D. Feldstein, R. Perea-Causín, Prof. E. Malic  
Division of Condensed Matter and Materials Theory  
Department of Physics  
Chalmers University of Technology  
Kemigården 1, Göteborg SE-412 96, Sweden

 The ORCID identification number(s) for the author(s) of this article can be found under <https://doi.org/10.1002/adma.202005254>.

© 2020 The Authors. Advanced Materials published by Wiley-VCH GmbH. This is an open access article under the terms of the Creative Commons Attribution-NonCommercial License, which permits use, distribution and reproduction in any medium, provided the original work is properly cited and is not used for commercial purposes.

DOI: 10.1002/adma.202005254



**Scheme 1.** Schematic representation of constructing BPNS-based covalent and noncovalent heterostructures.

of each component, and potentially generate new properties owing to the synergistic effect. In the heterostructures, the aggregation of BPNSs can also be reduced, so the intrinsic properties of BPNSs can be fully utilized. Thus far, BPNS-based heterostructures have found numerous applications such as in supercapacitors, batteries, field-effect transistors, catalytic water splitting, hydrogen or oxygen evolution reaction (HER or OER), biomedicine, and optoelectronics. It should also be mentioned that research on BPNS-based heterostructures is still at a very early stage, and several fundamental advances must be made, such as improved dispersibility and the development of efficient binding strategies. In 2018, Yang and Hao summarized BPNS-based 2D heterostructures, focusing exclusively on device applications.<sup>[76]</sup> The formation of heterostructures and the exploration of potential applications have become some of the next research hotspots for BPNSs. Critical discussions on recent progress in this field, especially from the last two years, are essential for further development. Here, we summarize recent efforts and progress in the development of BPNS-based 2D and 3D heterostructures and their applications. The critical problems encountered in the construction of heterostructures and potential future research directions are also discussed.

## 2. BPNS-Based Covalent and Noncovalent Heterostructures

### 2.1. BPNS-Based Covalent Heterostructures

The surface and/or edge functionalization of BPNSs obtained via forming covalent bonds with molecules/polymers is an effective means of passivating BPNSs and introducing new properties.<sup>[68,77,78]</sup> BPNSs utilize the lone pair of electrons present in the phosphorus and oxygen atoms existing in the hydroxyl group of oxidized phosphorus to constitute direct P–C and P–O–C covalent bonds, respectively.<sup>[72]</sup> Different chemical reactions have been developed for effective covalent functionalization of BPNSs, including free radical addition using diazonium chemistry<sup>[67]</sup> or the ball milling method,<sup>[71]</sup> nitrene addition,<sup>[79]</sup> and nucleophilic substitution.<sup>[80]</sup> Because

BPNSs are feasible for use in different organic reactions, they can be attached to other 2D materials to form heterostructures. Covalently attached 2D heterojunctions can be constructed by the edge functionalization of BPNSs with other 2D materials, whereas heterointerfaces can be formed by covalent interactions of the nanomaterials through the surface.<sup>[81–84]</sup> In addition to 2D heterostructures, 3D interconnected frameworks of BPNSs have been developed and have shown superior device and catalytic performance.<sup>[85–89]</sup> For instance, 3D crosslinked heterostructures were acquired by attaching carbon nanotubes (CNTs) to BPNSs using the ball milling method.<sup>[85–87]</sup> The CNTs were interposed between different layers of BPNSs to form a 3D interconnected structure, which prevents the self-restacking of BPNSs and improves lamellar conductivity. BPNSs can also be attached to other 2D materials by forming organic linkers, such as amide bonds, to obtain 3D assembled heterostructures.<sup>[88]</sup> As a result of directional layer-by-layer crosslinking, the 3D heterostructures improve the interfacial area and planarity between different layers. Recently, covalent P–O–C bond formation between BPNSs and graphene oxide (GO) nanosheets was found to reduce the voids and improve the alignment degree of the GO nanosheets, resulting in an excellent toughness and enhanced electrical conductivity.<sup>[90]</sup> So far, reports on the covalently attached heterostructures of BPNSs have been few and superficial. Because the covalently attached 3D networks possess the advantages of reduced self-restacking, a larger interfacial area, and porous structure, these materials are expected to be promising candidates for various applications, including energy storage and electrochemical or photochemical catalysis.

### 2.2. BPNS-Based Noncovalent Heterostructures

Owing to their large surface area with free electrons and negative zeta potential, BPNSs undergo various noncovalent interactions, such as those via van der Waals forces and electrostatic interactions with other 2D materials.<sup>[91–95]</sup> In most cases, different 2D materials are vertically stacked layer-by-layer to form heterointerfaces and horizontally grown to

yield heterojunctions through different noncovalent interactions. In general, BPNS-based noncovalent heterostructures are constructed using different methods, including mechanical exfoliation and dry transfer, CVD, and self-assembly from liquid-phase exfoliated dispersions. The first method forms van der Waals heterostructures through mechanical exfoliation, followed by the controlled transfer of different 2D layers through polymethylmethacrylate (PMMA) transfer,<sup>[96,97]</sup> polymethylglutarimide and PMMA transfer,<sup>[98]</sup> polyvinylalcohol (PVA) and PMMA transfer,<sup>[99]</sup> PDMS transfer,<sup>[100–104]</sup> and polycarbonate and PDMS transfer.<sup>[105]</sup> A 2D BPNS/ $\text{Al}_2\text{O}_3$ /BPNS van der Waals heterostructure was prepared by transferring two layers of mechanically exfoliated BPNSs using PDMS solid transfer and a layer of aluminum via electron beam evaporation.<sup>[106]</sup> A  $\text{SiO}_2$ /BPNS/ $\text{SiO}_2$  heterostructure was obtained through the PDMS transfer of BPNSs onto the Si/ $\text{SiO}_2$  surface, and another layer of  $\text{SiO}_2$  was sputtered over the entire sample.<sup>[107]</sup> In another method, a BPNS/ $\text{MoS}_2$ -based van der Waals heterojunction was constructed by CVD.<sup>[108]</sup> Another van der Waals heterojunction was constructed using the CVD of  $\text{MoS}_2$  on a  $\text{SiO}_2$ /p<sup>+</sup>-doped Si substrate, and then mechanically exfoliated BPNSs were transferred onto the  $\text{MoS}_2$  layer.<sup>[109]</sup> Apart from these techniques, several other methods have been used for the preparation of van der Waals heterostructures. For example, a BPNS/ $\text{TiO}_2$ /graphene hybrid hydrogel was prepared by dip-coating liquid exfoliated BPNSs onto a preprepared 3D  $\text{TiO}_2$ -graphene composite hydrogel.<sup>[110]</sup> Compared to other heterostructures, BPNS-based heterostructures need to be constructed in a glovebox to avoid oxidizing the BPNSs during processing.<sup>[111]</sup>

BPNS heterostructures can also be formed by electrostatically assembling BPNSs with other 2D materials that have an opposite zeta potential in solvents. For example, numerous BPNS-based heterostructures have been constructed by electrostatically assembling BPNSs with other 2D materials such as bismuth vanadate ( $\text{BiVO}_4$ ),<sup>[112]</sup> graphitic carbon nitride ( $\text{g-C}_3\text{N}_4$ ),<sup>[113]</sup> and MXene.<sup>[114]</sup> Ideally, highly ordered heterostructures can be obtained through the layer-by-layer assembly of differently charged nanosheets via electrostatic interactions. However, this is highly challenging owing to the poor solubility of heterostructures in various solvents.

Similar to BPNSs,<sup>[38]</sup> BPNS-based heterostructures can also be characterized by commonly used techniques such as Raman spectroscopy, transmission electron microscopy (TEM), atomic force microscopy (AFM), optical microscopy (OM), X-ray photoelectron spectroscopy (XPS), fluorescence (FL) spectroscopy, and X-ray diffraction (XRD). For example, the encapsulation of few-layer BPNSs using h-BN leads to a dramatic decline in the line width of the Raman bands of BPNSs because of the reduced phonon scattering rate.<sup>[115,116]</sup> A chemically crosslinked 3D structure of a BPNS-CNT hybrid was characterized using field emission scanning electron microscopy (FESEM) and TEM analysis.<sup>[85]</sup> The images showed that CNTs were interspersed and dispersed uniformly both on the surface and inside of the BPNSs, yielding a 3D interconnected BPNS-CNT heterostructure. Both the P2p and C1s spectra in the XPS measurements showed the presence of peaks corresponding to P-C and P-O-C bonds, indicating covalent bonds between the BPNSs and CNTs. However, with the currently available characterization techniques, it is still very challenging to provide solid

evidence on the covalent linkage of BPNS-based heterostructures and determine the exact structures.

### 3. Optical and Electronic Properties of BPNS-Based Heterostructures

Their extremely tunable bandgap covering infrared up to visible frequencies<sup>[52]</sup> (Figure 1a), highly anisotropic electronic dispersion,<sup>[117]</sup> optical properties<sup>[118]</sup> (Figure 1b,c), and optimal surface-to-volume ratio render BPNSs a promising material for several electronic and optoelectronic devices, such as transistors, gas sensors, and photodetectors.<sup>[119]</sup> The in-plane anisotropy of BPNSs provides new opportunities for novel electronic, photonic, and thermoelectric devices. The high (anisotropic) carrier mobilities and large on/off ratios at room temperature make BPNSs an excellent material for transistors, superior to graphene, which has a poor on/off ratio, and TMDs, which have low mobilities.<sup>[120]</sup>

Their remarkable optical and electronic properties lift BPNSs out of the shadow of graphene and TMDs. However, BPNSs undergo oxidation under ambient conditions. To overcome this obstacle to most technological applications, BPNSs can be protected by stacking other 2D materials on top, such as h-BN, graphene, or TMD monolayers. The layers within the 2D heterostructures are weakly bound via van der Waals interactions, preserving the properties of every single layer to a large extent. Protection from degradation is not the only motivation behind these BPNS-based van der Waals heterostructures. The vertical stacking of different 2D materials can also result in new functionalities that may be favorable for specific device applications. In contrast to van der Waals heterostructures, covalent bond formation on BPNSs has a p-doping effect because the electron pairs of phosphorus atoms are utilized for bond formation. It has also been reported that P-P bond breakage can occur in BPNSs as a result of nucleophilic substitution,<sup>[80]</sup> which can significantly change the electronic band structure. The optical properties of BPNS-based heterostructures are determined by the electronic band structure of these materials. The latter is very sensitive to the strength of interlayer coupling and hybridization. However, in the case of the noncovalent approach, the band structure of single layers remains unchanged to a considerable extent, preserving the optical properties of BPNSs. In the case of covalent functionalization, qualitative changes in the band structure and optical response of BPNS heterostructures are expected. Therefore, a delicate control of the degree of functionalization is normally required.

While there are many different BPNS-based heterostructures, herein, we focus on the optical and electronic properties of heterostructures consisting of BPNSs and different TMD (tungsten- and molybdenum-based) monolayers, graphene, and h-BN.

#### 3.1. BPNS/TMD Heterostructures

The main building blocks for many optoelectronic devices are p-n junctions. In conventional semiconductors, p-n homojunctions are formed by chemical doping, while p-n heterojunctions



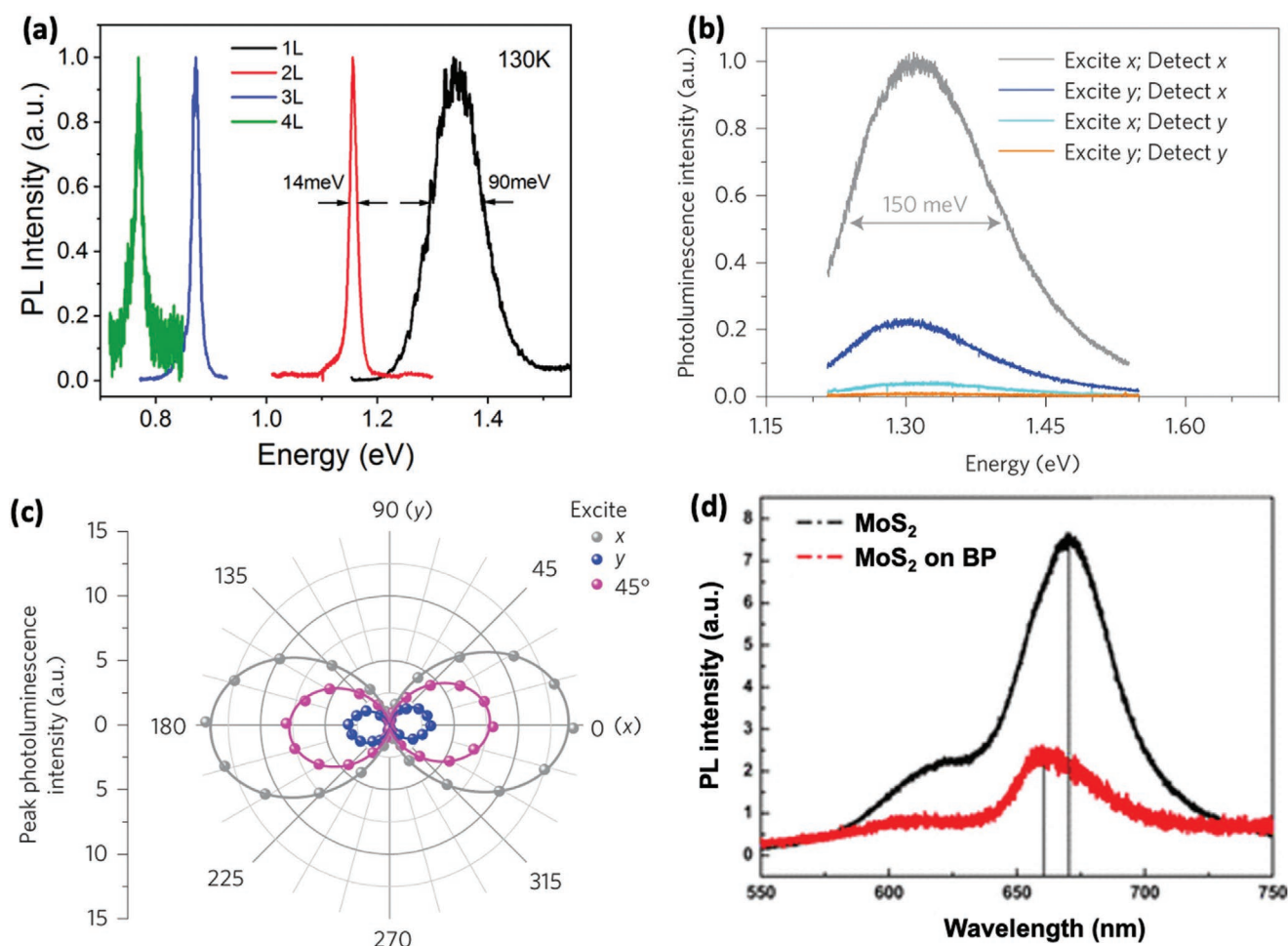


**Figure 1.** Optical properties of pristine BPNSs and BPNS/TMD heterostructures. a) Photoluminescence spectrum for mono-, bi-, tri-, and quadralayer BP samples. Reproduced with permission.<sup>[52]</sup> Copyright 2020, American Physical Society. b) The polarization-resolved photoluminescence spectrum of pristine BPNSs at room temperature shows a strong anisotropy of the emission, and c) photoluminescence peak intensity as a function of polarization detection angle. Reproduced with permission.<sup>[118]</sup> Copyright 2015, Springer Nature. d) The photoluminescence spectrum of BPNS/MoS<sub>2</sub> heterostructure exhibits a stronger quenching than the emission of MoS<sub>2</sub>. Reproduced with permission.<sup>[121]</sup> Copyright 2015, American Chemical Society.

can be created by growing an n-type semiconductor on a p-type semiconductor. Recently, an electrically tunable p–n heterojunction was developed based on few-layer BPNS/MoS<sub>2</sub> and BPNS/WS<sub>2</sub> van der Waals heterostructures using a PMMA-assisted liquid transfer method.<sup>[121]</sup> A type-II band alignment (staggered gap) was found for a BPNS/MoS<sub>2</sub> heterostructure with a band offset of 0.8 eV, which is comparable to the exciton binding energy. In contrast, BPNS–WS<sub>2</sub> is characterized by a type-I band alignment (straddling gap) owing to the larger bandgap of the WS<sub>2</sub> monolayer. Note that the band offset in a BPNS/TMD heterostructure can be considerably tuned by applying an external electric field.<sup>[122]</sup>

Characterization of the optical properties of BPNS/TMD heterostructures showed the drastic quenching of MoS<sub>2</sub> and WS<sub>2</sub> photoemissions (Figure 1d). Quenching is explained by an appearing built-in electric field that separates the Coulomb-bound electron–hole pairs, giving rise to a considerable reduction in the radiative recombination of excitons. Furthermore, a small blue shift of the MoS<sub>2</sub> and WS<sub>2</sub> resonances was observed, which is ascribed to the reduction of the bandgap within the

heterostructure. The emission of the few-layer BPNSs was expected at 0.3 meV and could not be resolved in the performed experiments. In another study, BPNSs, p-doped narrow-bandgap semiconductors, were combined with MoS<sub>2</sub> (as a large bandgap n-type semiconductor) to realize vertical van der Waals heterostructures simultaneously exhibiting very high rectifying (approaching 10<sup>6</sup>) and on/off ratios (up to 10<sup>7</sup>).<sup>[108]</sup>

### 3.2. BPNS/Graphene Heterostructures

Graphene can protect BPNSs from structural and chemical degradation through surface passivation and serve as an active layer for improving the contact of BPNSs with metal electrodes. Technologically important properties, such as direct bandgaps and in-plane anisotropy, have been shown to remain unchanged within the heterostructure.<sup>[123]</sup> First-principle calculations of the band structure resolving orbital contributions from BPNSs and graphene indicate that both the Dirac cone of graphene and the direct bandgap of BPNSs were preserved

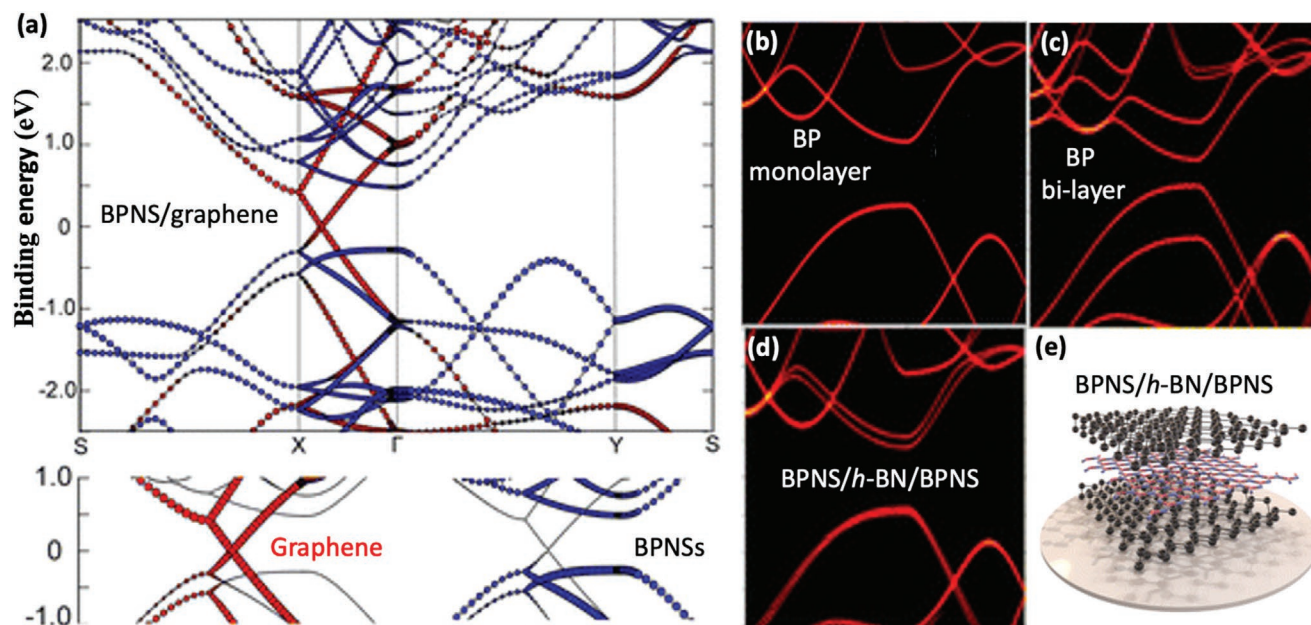


**Figure 2.** Change of the electronic band structure in BPNS/graphene and BPNS/h-BN heterostructures. a) The orbital-decomposed band structure of BPNS/graphene illustrates that the Dirac cone from graphene and the bandgap of BPNSs remain unchanged. Reproduced with permission.<sup>[123]</sup> Copyright 2015, American Chemical Society. Band structure of b) BP monolayer and c) BP bilayer shows a significant bandgap reduction. d) The band structure of the BPNS/h-BN/BPNS heterostructure reveals that the h-BN-spacer suppresses the bandgap reduction, and e) sketch of the BPNS/h-BN/BPNS stack. Reproduced with permission.<sup>[125]</sup> Copyright 2015, American Chemical Society.

(Figure 2a). A small bandgap opening of  $\approx 1$  meV was predicted due to the interruption of the structural symmetry in the heterostructure. Furthermore, by tuning the distance between the graphene and BPNSs, the Schottky barrier can be optimized for optoelectronic applications.<sup>[124]</sup> The Dirac point shifts from the conduction to the valence band (VB) of BPNSs as the interlayer distance is reduced from 0.45 to 0.28 nm, giving rise to a transition from an n-type to a p-type Schottky contact at the interface.

### 3.3. BPNS/h-BN Heterostructures

In addition to structural instability under ambient conditions, the decrease in the bandgap in BP stacks limits the quantum efficiency of BP-based devices because only monolayers can be used for near-infrared (NIR) optoelectronic applications. Constantinescu and Hine suggested that stacking monolayer BPNSs with h-BN, a large bandgap insulator can solve both problems simultaneously.<sup>[125]</sup> BPNSs were protected from degradation by h-BN encapsulation, resulting in a larger absorption efficiency without changing the bandgap of the BPNSs. The h-BN layer increased the separation of the BPNS layers and decreased their interlayer coupling. As a result, bilayer BPNSs behaved like a stack of two almost noninteracting BP monolayers, that is, the single-layer BP and the BPNS/h-BN/BPNS heterostructure showed a similar band structure; in particular, there was no significant decrease in the bandgap, as expected from a BP bilayer (Figure 2b–e). At the same time, the absorption efficiency can be significantly increased owing to the thick h-BN spaced BP multilayers. Furthermore, encapsulation with h-BN was shown to lead to a high on/off ratio exceeding  $10^5$  and a considerably

increased mobility value of up to  $4 \times 10^3 \text{ cm}^2 \text{ V}^{-1} \text{ s}^{-1}$  at low temperatures.<sup>[126]</sup> In another study, the passivation of BPNSs with atomically thin graphene and h-BN was investigated, demonstrating that the passivation preserved the pristine BP crystal structure under ambient conditions and concurrently enhanced the electron transport properties.<sup>[98]</sup> An in situ comparison of the transport properties of passivated and exposed areas of the same exfoliated BPNSs showed highly improved electron mobility (10–100-fold) for the passivated BPNSs and symmetrical electron and hole transconductance characteristics. A recent study investigated the impact of h-BN encapsulation on the structural and vibrational properties of few-layer BPNSs.<sup>[116]</sup> The encapsulation was found to flatten the puckered lattice structure of BPNSs by imposing a biaxial strain.

Overall, the optical and electronic properties of BPNSs and BPNS-based heterostructures have been well studied in recent years. However, while in the field of TMD- and graphene-based homo- and heterobilayers,<sup>[127–129]</sup> moiré exciton features resulting from misaligned monolayer lattices have moved into the focus of research, the impact of the moiré pattern on the optical and electronic properties of BPNS-based heterostructures has yet to be revealed.<sup>[130]</sup>

## 4. Applications of BPNS-Based Heterostructures

### 4.1. Electronic and Optoelectronic Applications

As discussed in the previous sections, BPNSs and BPNS-based heterostructures possess numerous remarkable properties including extremely tunable electronic bandgaps,

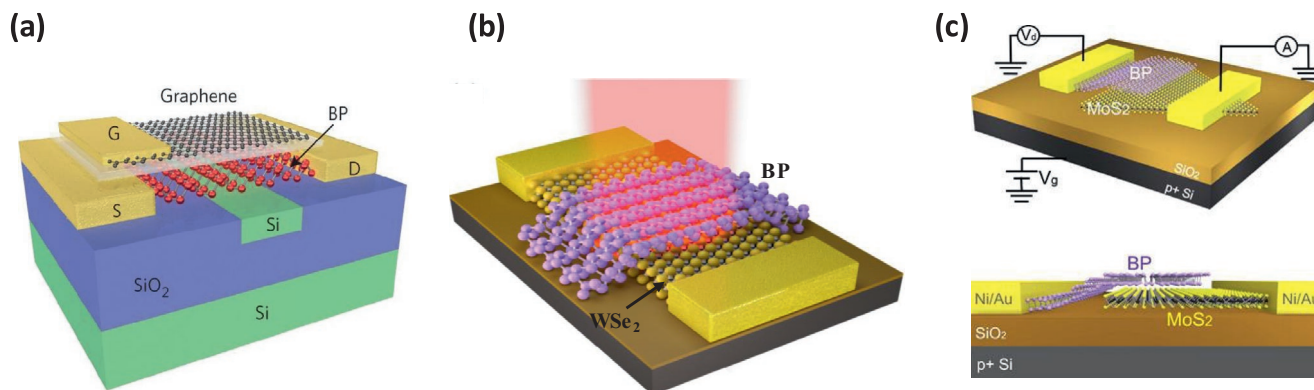


**Figure 3.** Schematic illustration of photodetector devices based on a) a BPNS/graphene heterostructure. Reproduced with permission.<sup>[145]</sup> Copyright 2015, Springer Nature. b) A BPNS/WSe<sub>2</sub> heterostructure. Reproduced with permission.<sup>[99]</sup> Copyright 2017, Elsevier. c) A BPNS/MoS<sub>2</sub> heterostructure. Reproduced with permission.<sup>[109]</sup> Copyright 2014, American Chemical Society.

highly anisotropic electronic and optical properties, and high carrier mobilities and on/off ratios, which make them promising materials for several technological applications, such as photodetectors, transistors, and gas sensors. The following sections contain a brief overview of the current status of selected applications based on BPNS/graphene, BPNS/h-BN, BPNS/TMD, and other BPNS-based heterostructures.

#### 4.1.1. Transistors

While graphene shows extremely high carrier mobilities, it exhibits very low on/off ratios owing to the lack of a bandgap. The TMDs exhibit high on/off ratios but possess relatively low carrier mobilities. In contrast, BPNSs possess both high mobilities and on/off ratios; therefore, they are suitable for applications in transistors. In 2014, the first field-effect transistor based on few-layer BPNSs with a thickness of just a few nanometers was fabricated.<sup>[120]</sup> A drain current adjustment of up to  $10^5$  and mobility of  $1 \times 10^3 \text{ cm}^2 \text{ V}^{-1} \text{ s}^{-1}$  were observed at room temperature, which is limited by electron–phonon scattering. These values surpassed those of a field-effect transistor based on few-layer BPNSs encapsulated in h-BN.<sup>[131]</sup> The field-effect transistor was characterized by remarkably high hole mobility of  $5.2 \times 10^3 \text{ cm}^2 \text{ V}^{-1} \text{ s}^{-1}$  at room temperature and even  $4.5 \times 10^4 \text{ cm}^2 \text{ V}^{-1} \text{ s}^{-1}$  at cryogenic temperatures. In the same year, a vertical field-effect transistor was reported based on a BPNS/graphene heterostructure, in which graphene was used as the bottom electrode to investigate out-of-plane charge transport in BPNSs.<sup>[132]</sup> The desired high on/off ratio values were shown to be limited by high off-currents owing to thermionic emission or tunneling through the graphene/BPNS Schottky barrier at high and low temperatures, respectively. Furthermore, field-effect transistors consisting of BPNS/h-BN/MoS<sub>2</sub> heterostructures were reported to operate as nonvolatile memory devices, where BPNSs act as a channel layer, while h-BN and MoS<sub>2</sub> serve as tunnel barriers and charge trapping layers, respectively.<sup>[101]</sup> The device showed a memory window as high as  $\approx 60 \text{ V}$  at a maximum control gate voltage of  $40 \text{ V}$ , which can be further regulated by varying the maximum control gate voltage. Recently, Kim et al. fabricated a BP heterojunction

tunnel field-effect transistor (BP-HJ-TFET) with a monolayer hexagonal boron nitride tunnel barrier for drain contact.<sup>[133]</sup> The BP-HJ-TFET showed a remarkable average subthreshold swing over four decades of current ( $SS_{\text{ave}_4 \text{ dec}}$ ) of  $37.6 \text{ mV dec}^{-1}$  at  $300 \text{ K}$  and high current of  $19.5 \mu\text{A } \mu\text{m}^{-1}$  at a subthreshold swing of  $60 \text{ mV dec}^{-1}$  ( $I_{60}$ ), providing a potential route for the development of ultrafast low power logic circuits.

In brief, BPNSs have optimal properties for realizing high-efficiency transistors. Building van der Waals heterostructures with other 2D materials, such as graphene or h-BN, can prevent the degradation of BPNSs and stabilize them in ambient conditions for high-performance transistors.<sup>[134–144]</sup>

#### 4.1.2. Photodetectors

BPNSs cover wide spectra ranging from visible to NIR and exhibit high carrier mobilities as well as a direct bandgap, resulting in efficient light absorption and low dark currents. These characteristics make BPNSs optimal candidates for highly efficient photodetectors. In 2015, a multilayer BPNS-based infrared photodetector integrated on a silicon photonic waveguide was demonstrated using few-layer graphene as the top-gate electrode (Figure 3a).<sup>[145]</sup> The photodetector was characterized by high responsivity (up to  $135 \text{ mA W}^{-1}$ ) and low dark currents (only  $220 \text{ nA}$ ) when gating BPNSs to low doping. The generated photocurrent was dominated by the photovoltaic effect in this system.

A photodetector based on a BPNS/graphene heterostructure operating in the NIR range and exhibiting an ultrahigh responsivity was recently reported.<sup>[146]</sup> Here, graphene acts as an encapsulation layer, improving the ambient stability of BPNSs. At the same time, it also serves as a highly efficient transport layer, which significantly reduces the Schottky barrier between the BPNSs and the metal electrodes, resulting in efficient photocurrent generation. The detector exhibited long-term stability, a high photoresponsivity of up to  $3.3 \times 10^3 \text{ A W}^{-1}$  at  $1550 \text{ nm}$ , and a polarization-dependent photocurrent response. Furthermore, a broadband photodetector with a high polarization sensitivity based on BPNS/WSe<sub>2</sub> heterostructures was also demonstrated (Figure 3b).<sup>[99]</sup> Here, BPNSs acted as the photogate, while WSe<sub>2</sub>



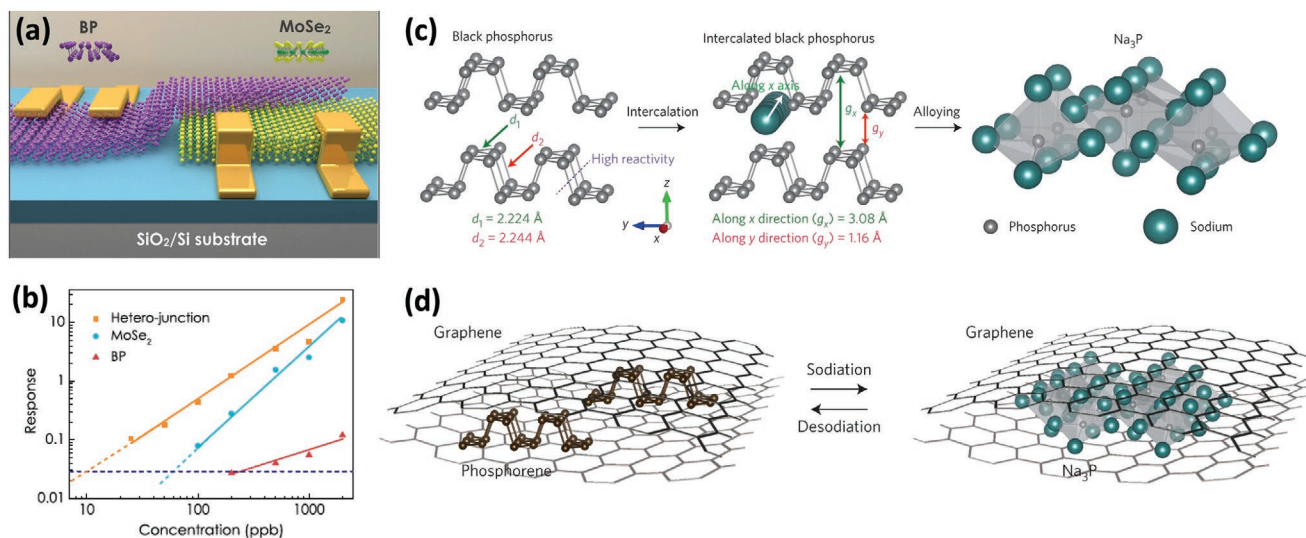


**Figure 4.** a) Schematic illustration of a photodetector device based on a BPNS/MoSe<sub>2</sub> heterostructure. b) Response of the heterostructure device compared with MoSe<sub>2</sub>- and BPNS-based devices as a function of gas concentrations. The intersection with the horizontal threshold line (blue dashed) corresponds to the detection limit of the device. Reproduced with permission.<sup>[155]</sup> Copyright 2016, IOP Publishing. c) Schematic illustration of BP before sodiation, with the first step of sodium-ion intercalation, and the second step of alloy reaction in sodium-ion batteries. d) Structural evolution of the BP/graphene heterostructure during sodiation. Reproduced with permission.<sup>[156]</sup> Copyright 2015, Springer Nature.

was the conductive channel. The optically excited charge carriers were divided by the built-in field created in the BPNS/WSe<sub>2</sub> heterostructure, which also efficiently reduced their radiative recombination. A photoresponsivity of up to  $10^3$  and  $5 \times 10^{-1} \text{ A W}^{-1}$  was measured for visible and infrared light, respectively. Broadband photodetectors have also been demonstrated based on BPNS/MoSe<sub>2</sub> heterostructures,<sup>[97,109,147]</sup> in which p-type BPNSs and n-type MoSe<sub>2</sub> constitute an atomically sharp p–n junction (Figure 3c). Furthermore, BPNS/InSe<sup>[96]</sup> and perovskite/BPNS/MoSe<sub>2</sub> heterostructures<sup>[148]</sup> have recently been developed to design broadband polarization-sensitive photodetectors characterized by fast response time and high responsivity. The photodetector device using a perovskite/BPNS/MoSe<sub>2</sub> heterostructure includes a vertically stacked BPNS/MoSe<sub>2</sub> photodiode modified with a perovskite layer on the top, operated under reverse or zero bias conditions based on photovoltaic and photogating mechanisms. Interestingly, the devices also showed impressive photovoltaic power conversion with a maximum external quantum efficiency of  $\approx 80\%$ , demonstrating their potential in both high-performance photodetection and efficient light energy harvesting devices.

In general, in addition to enhancing the stability of BPNS-based devices, BPNS-based heterostructures are beneficial because they enable electrically tunable p–n heterojunctions to be realized, facilitating the separation of photocarriers and improving the efficiency of photodetectors.<sup>[149]</sup>

#### 4.1.3. Sensors

The optimal surface-to-volume ratio of 2D materials renders them promising candidates for gas sensing because molecules can considerably change the electronic and optical properties of 2D materials.<sup>[150,151]</sup> DFT calculations showed that CO, H<sub>2</sub>, H<sub>2</sub>O, and NH<sub>3</sub> molecules act as electron donors, while NO, NO<sub>2</sub>, and

O<sub>2</sub> operate as electron acceptors when adsorbed on the surface of BP monolayers.<sup>[152]</sup> NO<sub>2</sub> was predicted to show the strongest interaction with BPNSs owing to efficient orbital hybridization. This was experimentally demonstrated by exposing BPNSs to different gases and measuring the change in the electrical resistance.<sup>[153,154]</sup>

A NO<sub>2</sub> chemical sensor based on few-layer BPNS/MoSe<sub>2</sub> heterostructures was developed,<sup>[155]</sup> exhibiting a very low detection limit and a much larger sensitivity compared to the pristine BPNS-based gas sensors (Figure 4a). This sensor was based on a new mechanism in which the band alignment at the BPNS/MoSe<sub>2</sub> interface sensitively changes upon exposure to NO<sub>2</sub>. The detection limit in terms of NO<sub>2</sub> gas concentration was found to be 10 parts per billion (ppb), which is much lower than both MoSe<sub>2</sub>- and BPNS-based sensors, which have a detection limit of 60 and 200 ppb, respectively (Figure 4b). Furthermore, compared with MoSe<sub>2</sub>- and BPNS-based sensors, the sensitivity of the BPNS/MoSe<sub>2</sub> heterostructure-based sensor is one order of magnitude higher. Interestingly, the difference in sensitivity becomes smaller compared to that of MoSe<sub>2</sub> sensors when the gas concentration increases, which might be due to the Schottky diode behavior of both sensors at high concentrations. In another study, a highly sensitive NO<sub>2</sub> sensor was fabricated based on a field-effect transistor with few-layer BPNSs, h-BN, and MoSe<sub>2</sub> acting as the top-gate, dielectric layer, and conduction channel material, respectively. Here, BPNSs serve as the sensing material, exploiting its excellent gas adsorption capability. The MoSe<sub>2</sub> conduction channel is isolated from the ambient environment by being covered with h-BN. The sensing mechanism is based on the charge transfer following the adsorption of NO<sub>2</sub> molecules on the gate material and changes in the resistance of the conduction channel material. The sensor showed a detection limit of 3.3 ppb.<sup>[157]</sup> Recently, Kim and co-workers constructed a heterostructure of BPNSs and holey few-layer graphene oxide ( $\approx 6.7 \text{ nm}$  thick) membranes.<sup>[158]</sup>



The ultrathin membranes acted as a multifunctional breathable passivation layer, shielding the BPNSs from oxidative degradation and allowing the selective diffusion of NO<sub>2</sub> molecules toward the underlying BPNSs. The heterostructure exhibited significantly enhanced NO<sub>2</sub> sensing performance under humid conditions with a rapid sensing response and excellent stability.

In short, BPNS-based heterostructures offer a high surface-to-volume ratio as well as a new highly sensitive detection mechanism for gases owing to the molecule-induced band alignment variation.

#### 4.2. Energy Storage Devices

Because of its puckered lattice structure, BP exhibits a larger interlayer spacing than graphite, allowing the intercalation of larger ions, which makes BPNSs promising for energy storage applications, including sodium-ion and lithium-ion batteries and supercapacitors.<sup>[56]</sup> Since 2007, BP-carbon composites have been used as anode materials in lithium-ion batteries and have shown improved charge capacity and first cycle efficiency compared to conventional graphite anode materials.<sup>[159]</sup> This concept was further improved by Sun et al.<sup>[84]</sup> BPNSs were also shown to improve the immobilization of sulfur, prolonging the cycle life of lithium-sulfur batteries. Furthermore, the addition of BPNSs to the cathode matrix remarkably accelerates the redox reactions for fast charging and discharging.<sup>[160]</sup> However, it was observed that during the charge/discharge processes, 2D crystal structures were destroyed as a result of huge volume changes, followed by a decrease of the electrical conductivity. During intercalation, phosphorus forms Li<sub>3</sub>P and Na<sub>3</sub>P, leading to a higher specific capacity, but a huge volume change resulted in the pulverization of the BPNSs after the first charge/discharge step. This problem can be resolved by constructing heterostructures with other 2D materials, as this can improve the interlayer distance and charge transfer properties via surface modification. For example, a heterostructure constructed by coating BPNSs onto a 3D porous graphene/TiO<sub>2</sub> composite hydrogel exhibited high electrochemical performance as an anode material for lithium-ion batteries.<sup>[110]</sup> The heterostructure showed an initial discharge capacity of 1336.1 mA h g<sup>-1</sup> at 0.2 A g<sup>-1</sup>, a rate capability of 271.1 mA h g<sup>-1</sup> at 5.0 A g<sup>-1</sup>, and a good cycling life of 502 mA h g<sup>-1</sup> over 180 cycles at a potential window near 3.0 V. The heterostructure benefitted from the reduced restacking of 2D nanosheets, improved interfacial charge storage and conductivity, shortened diffusion pathways, and suppressed volume changes during charge/discharge processes. Furthermore, Sun et al. fabricated a few-layer BPNS/graphene heterostructure to obtain high capacity and stable cyclability in sodium-ion batteries (Figure 4c,d).<sup>[156]</sup> Here, BPNSs facilitate a short diffusion path for sodium ions, while graphene acts as an electrical highway and mechanical backbone by providing an elastic buffer to accommodate the anisotropic expansion of the BPNS layers during sodiation. Recently, heterostructures consisting of BPNSs and MXenes have also been employed as anode materials for batteries.<sup>[114,161,162]</sup> For example, a BPNS/Ti<sub>3</sub>C<sub>2</sub> MXene heterostructure with stable fluorinated interphase was demonstrated as an efficient anode material for sodium storage batteries. The heterostructure facilitates the migration of both

electron and sodium ions and buffers the volume change of BPNSs during charge/discharge cycles. A reversible capacity of 535 mA h g<sup>-1</sup> at 0.1 A g<sup>-1</sup> and capacity (343 mA h g<sup>-1</sup> at 1 A g<sup>-1</sup>) retention of 87% over 1000 cycles was accomplished. Additionally, composites of BPNSs with carbon nanotubes,<sup>[163]</sup> graphene,<sup>[164,165]</sup> graphite,<sup>[84]</sup> graphite oxide,<sup>[84]</sup> carbon black,<sup>[84]</sup> and fullerene<sup>[84]</sup> were also studied for their superior electrochemical performances in batteries.

Compared to batteries, supercapacitors possess multiple advantages such as high power density, fast charge/discharge processes, and long cycle life.<sup>[166,167]</sup> To further enhance the capacitance performance, considerable attention should be paid to increasing conductivity and preventing the restacking of BPNSs. For example, a heterostructure of BPNSs chemically bridged to carbon nanotubes was demonstrated.<sup>[86]</sup> The heterostructure was then assembled into nonwoven fiber fabrics and used as electrode materials for flexible supercapacitors (Figure 5a). The supercapacitor, which was based on a mixture of CNTs and BPNSs that were chemically bonded to CNTs (CNT/BPNS-CNT), showed remarkable performance with an energy density of 96.5 mW h cm<sup>-3</sup>, a volumetric capacitance of 308.7 F cm<sup>-3</sup>, and 90.2% retention of the initial capacitance after 10 000 cycles, which was better than that of CNTs and a physical mixture of BPNSs and CNTs (BPNS/CNT) (Figure 5b). The performance was ascribed to the open layered structure of the BPNS/CNT heterostructure in addition to the lamellar electron conduction, mechanical stability, improved ionic pathways, and redox activity (Figure 5c,d). In another report, a single elemental heterostructure was constructed by combining BP and red phosphorus (RP) with excellent interfacial contact.<sup>[168]</sup> The BP/RP heterostructure exhibited improved electrochemical performance as electrode materials for both lithium-ion batteries and supercapacitors. From the recent progress, it is clear that the synthesis of BPNS-based heterostructures with suitable 2D materials holds great potential in improving the electrochemical performance in both batteries and supercapacitors by suppressing the volume change during the charge/discharge process, improving the interfacial charge transfer and storage, and enhancing electrical conductivity. In particular, building macroscopic (e.g., on 3D templates) and/or microscopic (e.g., crosslinking) 3D BPNS-based heterostructures is highly compelling for applications in high-performance energy storage devices.

#### 4.3. Photocatalytic Applications

Owing to their tunable direct bandgap, superior charge carrier mobility, large specific surface area, and a wide range of absorption from the visible to NIR region, BPNSs possess huge potential for use as metal-free photocatalysts.<sup>[70,169]</sup> Upon irradiation, BPNSs absorb photons with energies larger than or equal to their bandgap to form a photoexcited electron-hole pair.<sup>[170]</sup> Then, the excited electron-hole pair migrates to the surface of the photocatalyst and reduces or oxidizes the adsorbed substances at the interface. Although BPNSs are associated with favorable properties, considerable efforts have been made to overcome these drawbacks and enhance the photocatalytic activity by attaining long-lived electron-hole pairs via suppressed photoinduced charge carrier recombination, enhanced carrier

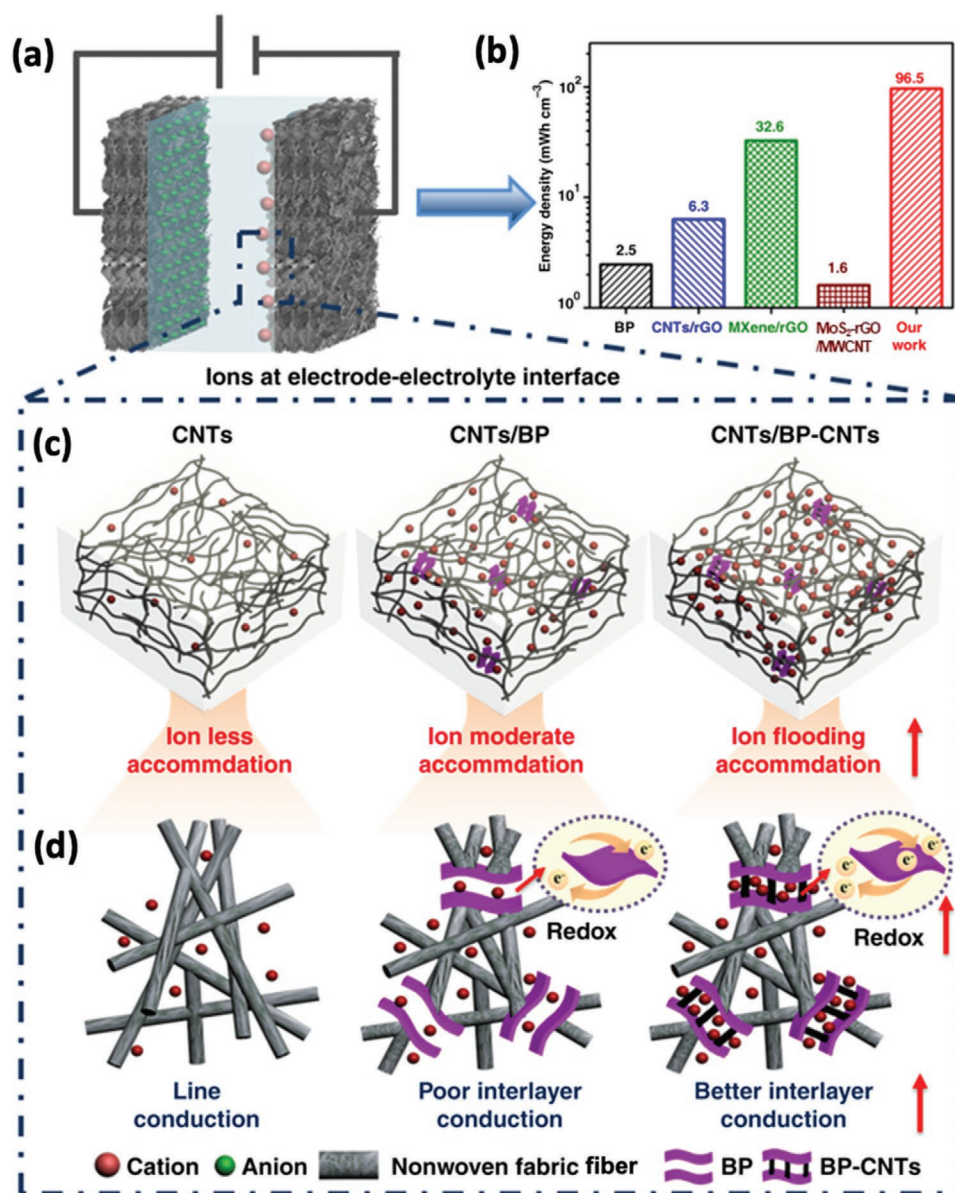


**Figure 5.** a) Schematic illustration of the flexible supercapacitor. b) Energy density of the supercapacitor based on a heterostructure of BPNSs chemically bridged to carbon nanotubes compared with that of other electrode-based supercapacitors (BP, CNTs/rGO, MXene/rGO, and MoS<sub>2</sub>-rGO/MWCNT). c) Charge distribution in three kinds of electrodes. d) Fine distribution of ions in three kinds of electrodes. Reproduced with permission.<sup>[86]</sup> Copyright 2018, Springer Nature.

mobility, optimized surface morphology for electron transfer, and improved ambient stability. Among the different functionalization strategies, the formation of heterostructures with suitable 2D materials is a promising way to engineer the optical and electronic properties of BPNSs. This section discusses BPNS-based heterostructures with improved photocatalytic activity toward hydrogen production, hydrogenation and oxidation reactions, and the removal of environmental pollutants.

Since the first report of H<sub>2</sub> production through photoelectrochemical water splitting using a TiO<sub>2</sub> catalyst,<sup>[171]</sup> the HER from water has been regarded as a promising method for transforming solar energy into chemical energy.<sup>[172]</sup> For complete water splitting reaction, the photocatalyst should have a more

negative conduction band minimum (CBM) than the redox potential of H<sup>+</sup>/H<sub>2</sub> (0 V vs normal hydrogen electrode (NHE)) and a more positive valence band maximum (VBM) than the redox potential of O<sub>2</sub>/H<sub>2</sub>O (1.23 V vs NHE), with a bandgap >1.23 eV.<sup>[170]</sup> Theoretical calculations indicate that BPNSs can be used for photocatalytic HER, but not for OER. The main challenge in pure 2D material photocatalysts is the fast charge recombination and thus poor performance. To this end, a heterostructure BPNS/g-C<sub>3</sub>N<sub>4</sub> with a P–N coordinated interfacial interaction was synthesized by stirring BPNSs and g-C<sub>3</sub>N<sub>4</sub> in *N*-methyl-2-pyrrolidone (NMP).<sup>[173]</sup> Compared with pure BPNSs and g-C<sub>3</sub>N<sub>4</sub>, an optimal BPNSs:g-C<sub>3</sub>N<sub>4</sub> ratio of 1:4 showed a higher H<sub>2</sub> evolution rate of 427 μmol g<sup>-1</sup> h<sup>-1</sup> using

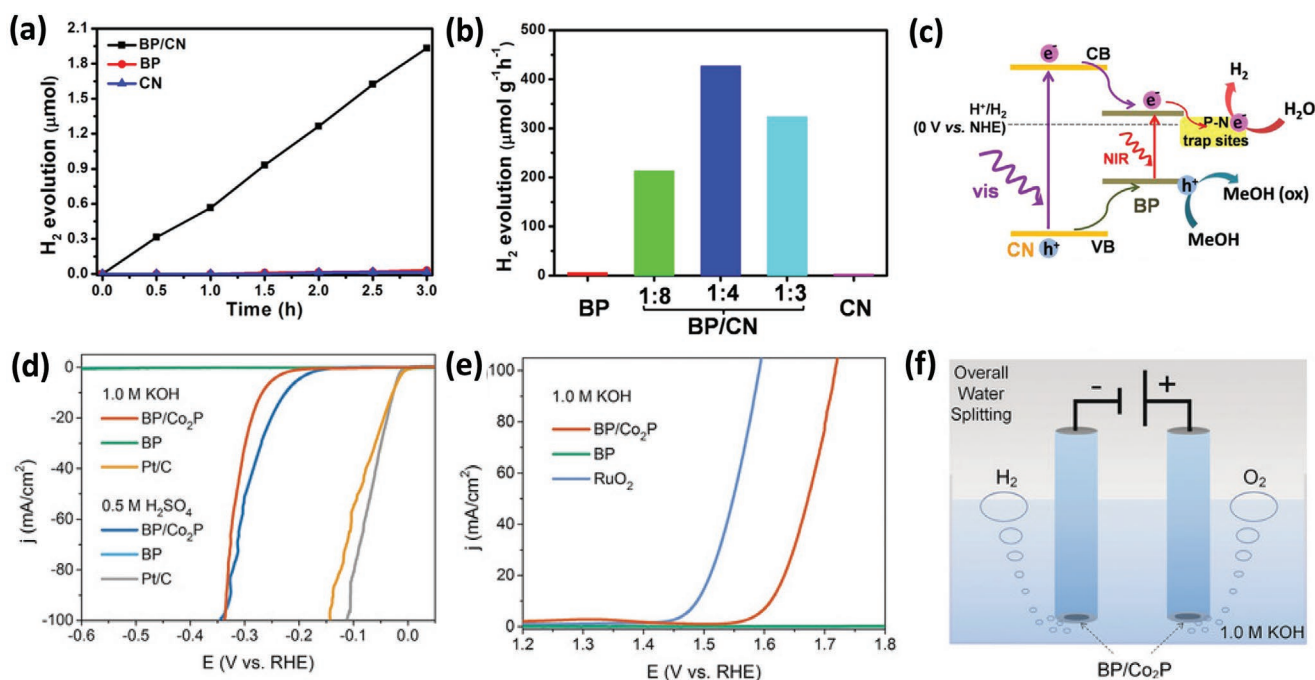


**Figure 6.** a) Photocatalytic H<sub>2</sub> evolution from water containing methanol (20 vol%) on different catalysts under visible light (>420 nm) irradiation. b) Effect of the BPNSs:CN ratio in the BPNS/CN heterostructure on the photocatalytic H<sub>2</sub> evolution rate under visible light irradiation for 3 h. c) Schematic diagram for the photocatalytic H<sub>2</sub> evolution using BPNS/CN. Reproduced with permission.<sup>[173]</sup> Copyright 2017, American Chemical Society. d) HER polarization curves of BPNSs, BPNS/Co<sub>2</sub>P heterostructure, and Pt/C in 0.5 M H<sub>2</sub>SO<sub>4</sub> and 1.0 M KOH. e) OER polarization curves of BPNSs, BPNS/Co<sub>2</sub>P heterostructure, and RuO<sub>2</sub> in 1.0 M KOH. f) Schematic diagram of the overall water splitting using BPNS/Co<sub>2</sub>P heterostructure. Reproduced with permission.<sup>[183]</sup> Copyright 2018, Wiley-VCH.

visible light (>420 nm) irradiation (Figure 6a,b). After repeated catalytic cycles followed by storage for two weeks, the heterostructure exhibited similar performance, indicating good photocatalyst stability. Owing to the broad absorption from the visible to NIR region, the heterostructure exhibited NIR light-driven photocatalytic activity (H<sub>2</sub> evolution rate of 101 μmol g<sup>-1</sup> h<sup>-1</sup>) using >780 nm light irradiation. Furthermore, the mechanism of photocatalytic activity was studied using various steady-state and time-resolved techniques. In the heterostructure, BPNSs act as an acceptor for electrons from the initially excited g-C<sub>3</sub>N<sub>4</sub>, which gives electrons to the conduction band (CB) of the BPNSs. Such electrons are trapped by the P–N coordination bond at the interface of the BPNSs and g-C<sub>3</sub>N<sub>4</sub>, leading to a long average lifetime for electrons and thus efficient H<sub>2</sub> generation (Figure 6c). Similarly, Ma and co-workers synthesized a 2D/2D heterojunction of BPNS/g-C<sub>3</sub>N<sub>4</sub> by assembling them in isopropanol and investigated their photocatalytic H<sub>2</sub> evolution performance.<sup>[113]</sup> Under λ > 420 nm light irradiation, BPNS/g-C<sub>3</sub>N<sub>4</sub> showed a H<sub>2</sub> evolution rate of 384.17 μmol g<sup>-1</sup> h<sup>-1</sup>, which is about 7 and 4.5 orders of magnitude higher than that of pristine BPNSs and g-C<sub>3</sub>N<sub>4</sub>, respectively. The improved photocatalytic performance of BPNS/g-C<sub>3</sub>N<sub>4</sub> compared to bare 2D nanosheets is ascribed to the suppressed charge recombination in g-C<sub>3</sub>N<sub>4</sub>, as the excited electrons in the CB of g-C<sub>3</sub>N<sub>4</sub> can be effectively transferred to BPNSs, which was exhibited by electrochemical impedance spectroscopy, transient photocurrent responses, and time-resolved photoluminescence studies. Qiao and co-workers reported a 2D/2D van der Waals heterojunction of BPNS/g-C<sub>3</sub>N<sub>4</sub> nanosheets constructed through physical mixing at room tem-

perature.<sup>[174]</sup> The heterojunction formed with an optimal content of 1.8 wt% BPNSs showed an enhanced photocatalytic hydrogen production activity of 571 μmol g<sup>-1</sup> h<sup>-1</sup>, which is even higher than that of Pt-loaded g-C<sub>3</sub>N<sub>4</sub> under identical conditions. The remarkable photocatalytic activity was due to the high efficiency interfacial charge transfer between the BPNSs and g-C<sub>3</sub>N<sub>4</sub> layers and the modified electronic structure of the BPNSs. Lu and co-workers constructed a Z-scheme (the stepwise charge transfer mechanism in natural photosynthesis) heterojunction of BPNS/monolayer Bi<sub>2</sub>WO<sub>6</sub> (MBWO) by decorating the surface of BPNSs with MBWO for photocatalytic H<sub>2</sub> production and the treatment of environmental pollution.<sup>[175]</sup> The 12 wt% BPNS:MBWO hybrid exhibited an enhanced photocatalytic performance in water splitting with the highest H<sub>2</sub> evolution rate of 21 042 μmol g<sup>-1</sup>, which is 9.15 orders of magnitude higher than that of the pristine MBWO. The heterostructure also showed remarkable photocatalytic activity for NO removal to purify air, and the NO removal ratio was as high as 67%, which is 2.6 times higher than that of pure MBWO. Moreover, a study on selectivity over other toxic gases could help achieve the full potential of the material, but the literature does not provide such details.

Developing stable and efficient photocatalysts for overall water splitting to H<sub>2</sub> and O<sub>2</sub>, excluding sacrificial reagents and external bias under visible light, is highly desirable. As the heterostructures combine the individual properties of different 2D materials, assembling 2D materials with water oxidation and reduction properties has received considerable attention as a means to obtain simultaneous water splitting to H<sub>2</sub> and



O<sub>2</sub> using solar energy. In this regard, Majima and co-workers constructed a Z-scheme heterostructure combining BPNSs and bismuth vanadate (BiVO<sub>4</sub>), acting as H<sub>2</sub> and O<sub>2</sub> production photocatalysts, respectively.<sup>[112]</sup> Upon photoexcitation, the photo-generated electrons in the CB of BiVO<sub>4</sub> rapidly recombined with the photogenerated holes in the VB of the BPNSs owing to their close band positions. Thus, the photogenerated electrons in the CB of the BPNSs spurred a reduction reaction, and the photogenerated holes in the VB of BiVO<sub>4</sub> sparked an oxidation reaction. In a similar photocatalytic charge transfer mechanism to photocatalytic hydrogen production, solar-driven photocatalytic reactions convert solar energy into chemical products, providing a promising approach to addressing the future energy crisis.<sup>[81,176–180]</sup> For example, Yu and co-workers prepared a novel semiconductor–metal heterostructure comprising BPNSs and ultrasmall Pt nanoparticles for photocatalytic hydrogenation and oxidation reactions.<sup>[81]</sup> The BPNS/Pt heterostructure exhibited a broad solar light absorption extending into the infrared region, efficient electron transfer with an ultrafast electron migration time of 0.11 ps, and further accumulation of photo-generated electrons on the ultrasmall Pt nanoparticles. These unique properties resulted in an extraordinary photocatalytic performance of BPNS/Pt in the hydrogenation of styrene and oxidation of benzyl alcohol. In short, heterostructures of BPNSs with other 2D materials further improve the photocatalytic activity of BPNSs owing to the reduced electron–hole recombination as a result of improved carrier mobility, effective charge transfer at the interface, and enhanced ambient stability.<sup>[181]</sup> Further studies on the charge transport and transfer mechanism in BPNS-based heterostructures can enable the design of more efficient photocatalysts in the future.<sup>[182]</sup>

#### 4.4. Electrocatalytic Applications

The electrocatalytic conversion of water into H<sub>2</sub> and O<sub>2</sub> has attracted widespread attention because of its high energy conversion efficiency and negligible environmental pollution.<sup>[184,185]</sup> The fabrication of efficient electrocatalysts for both HER and OER is required to facilitate an effective conversion. At present, the most effective catalysts for HER and OER are Pt-group metals and Ir/Ru-based compounds, respectively.<sup>[186–188]</sup> However, the high cost and lack of noble metal resources limit their practical applications. Owing to their large specific surface area with fully exposed surface atoms, long charge-carrier diffusion paths, higher charge carrier mobility, and active lone pairs, BPNSs are considered to be potential electrocatalysts for HER and OER.<sup>[189,190]</sup> The catalytic performance of BPNSs can be further improved by building BPNS-based heterostructures that provide numerous active sites (other electrocatalysts, electrons on the surface, or defects generated at the edges), high electrical conductivity, and efficient electron transfer. Yu and co-workers reported in-plane BPNS/Co<sub>2</sub>P heterostructures formed via a solvothermal process for electrocatalysis.<sup>[183]</sup> Co<sub>2</sub>P nanocrystals were selectively grown on the BPNS edges occupying the defects and provided effective electrocatalytic sites that improve electrocatalytic activities. The BPNS/Co<sub>2</sub>P heterostructure showed superior HER performance with onset overpotentials of 105 and 173 mV in 0.5 M H<sub>2</sub>SO<sub>4</sub> and 1.0 M KOH electrolytes, respectively

(Figure 6d). Furthermore, the OER activity of BPNS/Co<sub>2</sub>P was evaluated in 1.0 M KOH and showed a lower overpotential at 300 mV (Figure 6e) and a smaller Tafel slope of 78 mV dec<sup>−1</sup>, indicating the efficient OER activity of BPNS/Co<sub>2</sub>P. In addition, a device with a two-electrode configuration was fabricated with BPNS/Co<sub>2</sub>P as both the cathode and the anode for the overall water splitting reaction in 1.0 M KOH (Figure 6f). At 1.92 V, a current density of 10 mA cm<sup>−2</sup> was obtained for the electrode system in the polarization curve, demonstrating its potential as a water-splitting catalyst. In another report, Xu and co-workers fabricated a heterostructure forming a P–C covalent bond by ball milling activated graphene (AG) and BPNSs for supporting Ni<sub>3</sub>N particles in the application of OER.<sup>[82]</sup> The Ni<sub>3</sub>N/BP–AG heterostructure exhibited an OER performance with an overpotential of 233 mV at a current density of 10 mA cm<sup>−2</sup> and a Tafel slope of 42 mV dec<sup>−1</sup>. The catalysts also showed good stability, as the initial current density remained over 86.4% after measuring for 10<sup>4</sup> s. Moreover, the Ni<sub>3</sub>N/BP–AG heterostructure also exhibited better electrocatalytic OER performance than the commercial Ru- and Ir-based catalysts.

To enhance the ambient stability and explore the intrinsic catalytic activity of BPNSs, Dai and co-workers constructed a metal-free heterostructure electrostatically combining BPNSs and higher Fermi level N-doped graphene (NG).<sup>[189]</sup> The heterostructure acted as a bifunctional catalyst for overall water splitting and showed a remarkably low cell voltage of 1.54 V at a current density of 10 mA cm<sup>−2</sup> in an optimized electrolyzer. From the combined theoretical and experimental results, it was conceived that electronic interactions at the heterointerface should lead to electron transfer from NG to BPNSs (low Fermi level). As a result, electrons accumulate over the surface of the BPNSs and act as active sites that stabilize the adsorbed H of HER in the heterostructure. The interfacial charge transfer also induces charge relocation and positively charged carbon sites across the interface, facilitating the adsorption of OER intermediates. Among the 2D materials, MoS<sub>2</sub>-based electrocatalysts have attracted considerable attention owing to their large number of active sites at the edges.<sup>[191,192]</sup> Unfortunately, MoS<sub>2</sub> has a lower intrinsic exchange current density, which is another key factor for HER activity and can be improved by accumulating electrons on MoS<sub>2</sub> catalysts. Zeng and co-workers constructed a heterostructure by depositing MoS<sub>2</sub> flakes on BPNSs.<sup>[27]</sup> Because of the higher Fermi level of BPNSs, electrons are transferred from BPNSs to MoS<sub>2</sub> in the heterostructure with an intrinsic exchange current density of 0.66 mA cm<sup>−2</sup>, which is 22-fold higher than that of MoS<sub>2</sub>. The heterostructure also showed increased HER activity with an overpotential as low as 85 mV at a current density of 10 mA cm<sup>−2</sup>.

Because of their excellent electronic properties, BPNSs were combined with anatase titanium dioxide nanosheets by ball milling to obtain an anatase titanium dioxide nanosheet–BP heterostructure (ATN–BP), which was used as a support for Pd nanoparticles in ethanol oxidation reactions (EORs).<sup>[193]</sup> In the ATN–BP heterostructure, the BPNSs are interconnected by ATN via P–O–Ti bonds, which improves the electrolyte penetration and electron transportation and improves the stripping of reactive intermediates. In an alkaline medium, the Pd/ATN–BP heterostructure showed an electrochemically active surface area of 462.1 m<sup>2</sup> g<sub>Pd</sub><sup>−1</sup> and a mass peak current



density of 5023.8 mA mg<sub>Pd</sub><sup>-1</sup>, which are 11.67 and 6.87 orders of magnitude higher than those of commercial Pd/C, respectively. In addition, the catalyst exhibited enhanced stability with a retention rate of the peak current density  $\approx 30.6\%$  after  $3.6 \times 10^3$  s, which is much higher than other Pd catalysts. The BPNSs form a suitable heterointerface with ATN nanosheets to support metal catalysts, which improves the electrochemical activity of the metal catalysts. Overall, compared with their bare materials, BPNS-based heterostructures show better electrocatalytic performance for electrocatalysis. An in-depth understanding of the mechanistic aspects of electrocatalysis in BPNS-based heterostructures is still lacking and requires additional experimental and theoretical studies.

#### 4.5. Biological Applications

Compared with other 2D nanomaterials, BPNSs exhibit excellent biodegradability and biocompatibility and hold great potential for use in biological applications.<sup>[196–198]</sup> The efficient drug loading provided by the large specific surface area, high photothermal conversion efficiency owing to the intense absorption in the NIR region, ease of degradable and nontoxic nature, and direct bandgap have made BPNSs potentially suitable as nanoagents in bioimaging, photothermal therapy, photodynamic therapy, and drug delivery systems.<sup>[199–203]</sup> Recently, efforts have been made to develop multifunctional BPNS-based heterostructures for bioapplications. A biocompatible BPNS/Bi<sub>2</sub>O<sub>3</sub> heterostructure was constructed as a radiosensitizer for X-ray induced photodynamic therapy (X-ray-PDT), which is a promising approach for synergistic cancer radiotherapy.<sup>[194]</sup> In contrast to conventional PDT with visible or NIR irradiation, X-ray-PDT provides deep tissue penetration in cells and thus provides better cancer treatment.<sup>[204,205]</sup> Because BPNSs cannot be directly excited by X-rays, a heterostructure composed of BPNSs and a material with high Z element Bi have been synthesized by growing Bi<sub>2</sub>O<sub>3</sub> nanoparticles on BPNSs. High Z elements with large photoelectric cross sections are known to produce reactive oxygen species (ROS) and to transfer energy to 2D sensitizers for increased ROS production.<sup>[206,207]</sup> Compared with bare BPNSs, Bi<sub>2</sub>O<sub>3</sub> more effectively passivates BPNSs both in water and in the solid state. The synergistic effects of BPNSs and Bi<sub>2</sub>O<sub>3</sub> enable efficient singlet oxygen (<sup>1</sup>O<sub>2</sub>) overproduction under X-ray irradiation via a Z-scheme photosensitized system, providing increased radiotherapy activity toward A375 cancer cells by inducing cell apoptosis and cycle arrest. In vivo BPNS/Bi<sub>2</sub>O<sub>3</sub> sensitized radiotherapy in melanoma xenograft nude mice demonstrated enhanced tumor inhibition effects and good biocompatibility between the P and Bi elements. The BPNS/Bi<sub>2</sub>O<sub>3</sub> sensitizer averts the drawbacks of conventional PDT, and the excellent biocompatibility of BPNSs improves the overall performance of the X-ray-PDT. Furthermore, the development of such heterostructures using BPNSs functionalized with cancer cell receptor molecules could enhance cellular uptake and improve localized cancer treatment without affecting normal cells.

The degradation products of BPNSs can be transformed in situ into P-based agents capable of promoting bone regeneration.<sup>[195,208]</sup> To this end, a bifunctional BPNS-reinforced

3D-printed bioglass scaffold (BP/BG) was constructed by integrating BPNSs into the surface of a bioglass scaffold for photothermal therapy of osteosarcoma and the subsequent bone regeneration.<sup>[195]</sup> After implanting the BP/BG scaffold into mouse osteosarcoma tissues, BPNS photothermal therapy enforces hyperthermia-induced osteosarcoma ablation. The oxidation of BPNSs releases a large amount of PO<sub>4</sub><sup>3-</sup>, and then the biomineralization reaction extracts calcium ions from the physiological environment, which accelerates the formation of new calcium phosphate (CAP) nanoparticles to establish bone regeneration (Figure 7). A study in male Sprague-Dawley rats showed that BP–BG scaffolds exhibited much better bone defect repair performance than the pure BG scaffolds. Owing to the ease of biodegradation and the nontoxicity of phosphorus-based products in physiological environments, BPNSs can be a better candidate for biological applications than other 2D materials such as TMDs. However, the instability of BPNSs in body fluids greatly hampers beneficial properties such as photothermal efficiency and carrier mobility. In general, the remarkable biocompatibility, a wide range of absorption, high photothermal efficiency, and good carrier mobility of BPNSs are inherited from the heterostructures, which can provide novel multifunctional materials with improved properties for bioapplications.

## 5. Conclusions and Outlook

The construction and applications of heterostructures are the next hotspots in BPNS-based research. In this progress report, we have outlined the recent advances in the formation of BPNS-based 2D and 3D heterostructures via covalent or noncovalent strategies and their electronic, optoelectronic, energy storage, catalytic, and biological applications (Table 1). A concise perspective on state-of-the-art research and future directions in BPNS-based heterostructures are discussed in this section.

### 5.1. Construction of Covalent and Noncovalent 2D and 3D Heterostructures

The covalent bonding of BPNS with other 2D materials via phosphorus and/or oxygen atoms provides stable edge and/or surface-functionalized BPNSs with integrated properties. 3D crosslinked heterostructures were obtained by forming strong P–C bonds via BPNS ball milling with other nanomaterials. Such 3D networks possess the advantages of reduced self-restacking, improved conductivity, a higher interfacial area, and porous structures and have been used in energy storage and catalysis applications. 3D assembled heterostructures can also be obtained from a layer-by-layer crosslinking of 2D materials using wet chemical routes, but the poor dispersibility of the heterostructures will limit the growth of more covalently linked layers. In addition, attaining a regular array of different 2D layers is also necessary, but this could be done via the suitable functionalization of nanosheets through directional bond formation. Most BPNS-based heterostructures have been constructed via noncovalent interactions such as van der Waals forces and electrostatic interactions. However, van der Waals

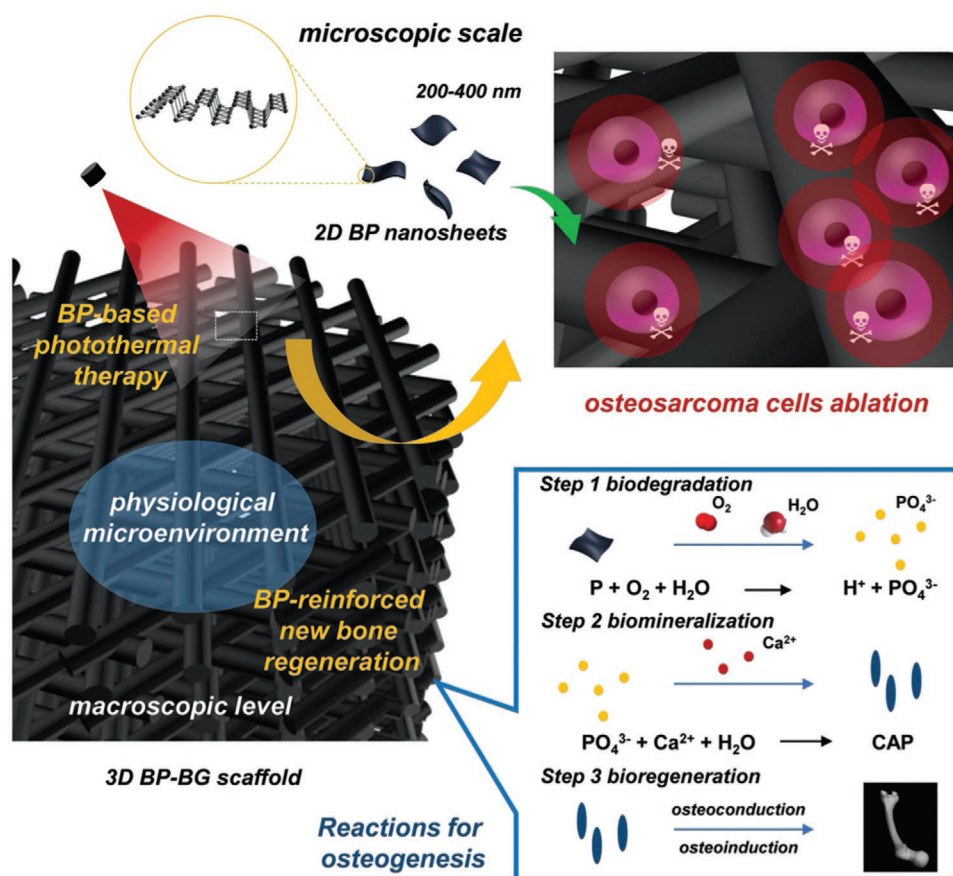


**Figure 7.** Schematic illustration of a stepwise therapeutic strategy for the elimination of osteosarcoma followed by osteogenesis using a BP/BG 3D heterostructure. Reproduced with permission.<sup>[195]</sup> Copyright 2018, Wiley-VCH.

heterostructures with interlayer discrepancies, such as variable interlayer distances and twist angles between the layers, and different thicknesses, can lead to heterostructures with varying properties from sample to sample. This could be addressed by finding new synthetic methods for heterostructures with atomically sharp interfaces. Functionalized BPNSs with positive or negative zeta potentials more easily form heterostructures with oppositely charged nanomaterials through electrostatic interactions in solutions, but the poor solubility of heterostructures again hinders the formation of more layers. It should also be mentioned that the large-scale preparation of stable BPNSs is still a challenge, which further limits the construction of heterostructures for practical applications. As the field of BPNS-based heterostructures grows, it is very important to develop new scalable synthetic methods in which the properties of each material can be preserved and the number of layers can be controlled. Furthermore, the layer-by-layer array of more than two different nanosheets will be more appealing for the construction of next-generation BPNS-based 2D and 3D heterostructures with long-term stability. Interestingly, organic molecules/BPNS heterostructures have been recently demonstrated using a self-assembly approach, which is a direction rarely explored.<sup>[209]</sup>

When comparing covalent and noncovalent approaches and their impact on heterostructures, it is very important to

use the appropriate preparation methods to obtain heterostructures with targeted performance. In general, noncovalent heterostructures can greatly preserve the properties of BPNSs and add additional functionality by stacking other materials on top. In contrast, the formation of covalent bonds significantly changes crystal lattices and electronic band structure. Therefore, for covalent approaches, critical control over the degree of functionalization is required to maintain the properties of BPNSs to avoid unwanted functionalization and lattice destruction.

## 5.2. Catalytic Applications

In contrast to other 2D materials, the presence of a direct bandgap, higher charge transport properties, and a wide range of absorption from the ultraviolet–visible to NIR region gives BPNSs potential as a photocatalyst. Importantly, BPNSs have a more negative CBM than the redox potential of  $H^+/H_2$ , so they can be used as photocatalysts for hydrogen production. BPNS-based heterostructures reach a charge separation with a longer lifetime and efficient charge transfer between different 2D layers by suppressing fast charge recombination to enhance the overall photocatalytic performance. However, the exact mechanism involved in the charge transfer and transport at the

**Table 1.** Summary of BPNS-based heterostructures, the type of interactions, and applications.

Heterostructure	Type of interaction	Application	Refs.
h-BN/BPNS/h-BN	van der Waals interaction	Transistor	[131]
BPNS/graphene	van der Waals interaction	Transistor	[132]
BPNS/h-BN/MoS <sub>2</sub>	van der Waals interaction	Transistor	[101]
BPNS/h-BN	van der Waals interaction	Transistor	[133]
BPNS/graphene	van der Waals interaction	Photodetector	[145,146]
BPNS/WSe <sub>2</sub>	van der Waals interaction	Photodetector	[99]
BPNS/MoS <sub>2</sub>	van der Waals interaction	Photodetector	[97,109,147]
BPNS/InSe	van der Waals interaction	Photodetector	[96]
Perovskite/BPNS/MoS <sub>2</sub>	van der Waals interaction	Photodetector	[148]
BPNS/MoSe <sub>2</sub>	van der Waals interaction	Gas sensor	[155]
BPNS/h-BN/MoS <sub>2</sub>	van der Waals interaction	Gas sensor	[157]
BPNS/graphene/TiO <sub>2</sub>	van der Waals interaction	Lithium ion batteries	[110]
BPNS/graphene	van der Waals interaction	Sodium ion batteries	[156]
BPNS/Ti <sub>3</sub> C <sub>2</sub> MXene	Electrostatic interaction	Sodium ion batteries	[114]
BPNS/Ti <sub>3</sub> C <sub>2</sub> T <sub>x</sub> MXene	van der Waals interaction	Sodium ion batteries	[161]
BPNS/V <sub>2</sub> CT <sub>x</sub> MXene	van der Waals interaction	Potassium ion batteries	[162]
BPNS/CNTs	Covalent bond	Supercapacitor	[86]
BP/RP	van der Waals interaction	Lithium ion batteries and supercapacitors	[168]
BPNS/g-C <sub>3</sub> N <sub>4</sub>	Coordination bond	Photocatalytic hydrogen evolution	[173]
BPNS/g-C <sub>3</sub> N <sub>4</sub>	van der Waals interaction	Photocatalytic hydrogen evolution	[174]
BPNS/g-C <sub>3</sub> N <sub>4</sub>	Electrostatic interaction	Photocatalytic hydrogen evolution	[113]
BPNS/MBWO	van der Waals interaction	Photocatalytic water splitting and NO removal	[175]
BPNS/BiVO <sub>4</sub>	Electrostatic interaction	Photocatalytic water splitting	[112]
BPNS/Pt	Covalent bond	Photocatalytic hydrogenation and oxidation reactions	[81]
BPNS/Co <sub>2</sub> P	van der Waals interaction	Electrocatalytic water splitting	[183]
Ni <sub>3</sub> N/BPNS/graphene	Covalent bond	Electrocatalytic oxygen evolution reaction	[82]
BPNS/TiO <sub>2</sub>	Covalent bond	Electrocatalytic ethanol oxidation	[193]
BPNS/Bi <sub>2</sub> O <sub>3</sub>	van der Waals interaction	Cancer radiotherapy	[194]
BPNS/3D printed bioglass	van der Waals interaction	Photothermal therapy of osteosarcoma and bone regeneration	[195]

interfaces is still unclear and requires further investigation in both theoretical and experimental research.<sup>[210]</sup> Compared to bare BPNSs, the electrocatalytic performance of BPNS-based heterostructures was found to be superior because of the large number of active sites, improved electrical conductivity, and efficient electron transfer. BPNS-based heterostructures are currently highly promising candidates for both photo- and electrocatalytic applications.

### 5.3. Energy Storage Applications

To date, BPNSs have attracted considerable attention for their outstanding energy storage performance. BPNS-based heterostructures were found to limit serious volume changes and prevent aggregation during the fast charge/discharge process in batteries. To this end, heterostructures with flexible covalent bonds would be an efficient candidate because the flexible bonds can resist bond breakage and thus prevent the degradation of BPNSs during charge/discharge cycles. BPNS-based

heterostructures provide increased conductivity and a larger surface area by avoiding the restacking of BPNSs, resulting in better electrochemical performance.

### 5.4. Biological Applications

Owing to the outstanding biocompatibility, biodegradability, and photothermal and photosensitizing properties of BPNSs, BPNS-based heterostructures hold great potential for biological applications. The nontoxic degradation products of BPNSs in the heterostructures were also found to undergo biomineralization to initiate bone regeneration. However, the degradation of BPNSs in the physiological environment reduces their photothermal and photosensitizing activity. BPNSs have also been reported to generate ROSs via energy transfer in the pristine state or synergistically in the heterostructures. As an advanced strategy, heterostructures of BPNSs functionalized with cancer-targeted molecules could further improve site-selective activity during cancer treatment.

## 5.5. Optical and Electronics Applications

In terms of understanding their optical and electronic properties, the moiré exciton features in BPNS-based heterostructures resulting from misaligned monolayer lattices have not yet been investigated thoroughly. The twist angle between two vertically stacked layers can be used to more finely tune the fundamental properties of the heterostructure. The spatially dependent, periodic moiré potential gives rise to arrays of trapping potentials and can lead to flat excitonic bands and even superconductivity, as recently shown for twisted bilayer graphene.<sup>[128]</sup> Exciton formation, thermalization, and decay dynamics, the hybridization effects of intra and interlayer excitons,<sup>[129]</sup> exciton diffusion,<sup>[211]</sup> and dissociation at interfaces in BPNS/TMD heterostructures are additional topics that need to be explored in future studies. In terms of electronic and optoelectronic applications, tunable bandgaps covering infrared to visible frequencies, high carrier mobilities, and large on/off ratios at room temperature lift BPNS-based heterostructures out of the shadow of graphene and TMDs. Within a relatively short time, significant progress has already been made in exploiting the potential of BPNSs for various electronic and optoelectronic applications, including high-performance transistors, infrared photodetectors, and gas sensors. Small-size BPNS samples obtained via mechanical exfoliation have been used to perform proof-of-concept studies; however, the production of high-quality, large-scale samples of BP monolayers and BP-based heterostructures, which is a crucial prerequisite for realistic commercial electronic and optoelectronic applications, has yet to be realized. The CVD growth of BPNS-based heterostructures might be a good option for further explanation.<sup>[212]</sup> In addition, to optimize the operational performance of gas sensors, a better microscopic understanding of the many-particle processes behind the generation of currents in novel photodetectors using BPNS-based heterostructures is necessary, as are microscopic insights into new interaction channels introduced through coupling BPNSs with molecules in a BPNS-based heterostructure. Recently, BPNS-based heterostructures were also found to be highly promising for electrically driven mid-infrared (MIR) light emission.<sup>[213,214]</sup> In another report, a light-emitting diode (LED) fabricated with a BPNS/MoS<sub>2</sub> heterojunction showed polarized electroluminescence at  $\lambda = 3.68 \mu\text{m}$ , with internal and external quantum efficiencies of  $\approx 1\%$  and  $\approx 0.03\%$ , respectively, at room temperature.<sup>[213]</sup> Because the bandgap of BPNSs can be easily tuned with respect to thickness, vertical electrical bias, chemical doping, BPNSs, and their heterostructures are attractive candidates for versatile MIR light sources.

In conclusion, recent advances in the synthesis and applications of BPNS-based heterostructures are highly promising but are still in their embryonic stages. In the coming years, BPNS-based 2D, and especially, 3D heterostructures are expected to be studied extensively to obtain efficient synthetic methods and to gain more knowledge about their properties and relevant applications.

## Acknowledgements

X.Z. would like to thank the financial support from “Stiftelsen Chalmers Tekniska Högskola,” “Helge Ax:son Johnsons Stiftelse,” (F19-0050), and Adlerbertska Forskningsstiftelsen (C 2020-1230) and Göteborg Energi (Tänk:Om Stipendiet). E.M. acknowledges funding from the Swedish

Research Council (VR, project number 2018-00734) and the European Union Horizon 2020 research and innovation programme under grant agreement no. 881603 (Graphene Flagship).

## Conflict of Interest

The authors declare no conflict of interest.

## Keywords

2D structures, 3D networks, black phosphorus, heterostructures

Received: August 3, 2020

Revised: October 8, 2020

Published online:

- [1] P. Das, Q. Fu, X. Bao, Z.-S. Wu, *J. Mater. Chem. A* **2018**, *6*, 21747.
- [2] P. Solís-Fernández, M. Bissett, H. Ago, *Chem. Soc. Rev.* **2017**, *46*, 4572.
- [3] B. Luo, G. Liu, L. Wang, *Nanoscale* **2016**, *8*, 6904.
- [4] H. Wang, F. Liu, W. Fu, Z. Fang, W. Zhou, Z. Liu, *Nanoscale* **2014**, *6*, 12250.
- [5] D. Jariwala, T. J. Marks, M. C. Hersam, *Nat. Mater.* **2017**, *16*, 170.
- [6] A. C. Ferrari, F. Bonaccorso, V. Fal'ko, K. S. Novoselov, S. Roche, P. Bøggild, S. Borini, F. H. L. Koppens, V. Palermo, N. Pugno, J. A. Garrido, R. Sordan, A. Bianco, L. Ballerini, M. Prato, E. Lidorikis, J. Kivioja, C. Marinelli, T. Ryhänen, A. Morpurgo, J. N. Coleman, V. Nicolosi, L. Colombo, A. Fert, M. Garcia-Hernandez, A. Bachtold, G. F. Schneider, F. Guinea, C. Dekker, M. Barbone, Z. Sun, C. Galiotis, A. N. Grigorenko, G. Konstantatos, A. Kis, M. Katsnelson, L. Vandersypen, A. Loiseau, V. Morandi, D. Neumaier, E. Treossi, V. Pellegrini, M. Polini, A. Tredicucci, G. M. Williams, B. Hee Hong, J.-H. Ahn, J. Min Kim, H. Zirath, B. J. van Wees, H. van der Zant, L. Occhipinti, A. Di Matteo, I. A. Kinloch, T. Seyller, E. Quesnel, X. Feng, K. Teo, N. Rupesinghe, P. Hakonen, S. R. T. Neil, Q. Tannock, T. Löfwander, J. Kinaret, *Nanoscale* **2015**, *7*, 4598.
- [7] C. Tan, X. Cao, X.-J. Wu, Q. He, J. Yang, X. Zhang, J. Chen, W. Zhao, S. Han, G.-H. Nam, M. Sindoro, H. Zhang, *Chem. Rev.* **2017**, *117*, 6225.
- [8] Y. Liu, H. Wang, S. Wang, Y. Wang, Y. Wang, Z. Guo, S. Xiao, Y. Yao, Q. Song, H. Zhang, K. Xu, *Adv. Opt. Mater.* **2020**, *8*, 1901526.
- [9] A. K. Geim, I. V. Grigorieva, *Nature* **2013**, *499*, 419.
- [10] E. Pomerantseva, Y. Gogotsi, *Nat. Energy* **2017**, *2*, 17089.
- [11] J.-H. Chen, C. Jang, S. Xiao, M. Ishigami, M. S. Fuhrer, *Nat. Nanotechnol.* **2008**, *3*, 206.
- [12] L. Wang, I. Meric, P. Y. Huang, Q. Gao, Y. Gao, H. Tran, T. Taniguchi, K. Watanabe, L. M. Campos, D. A. Muller, J. Guo, P. Kim, J. Hone, K. L. Shepard, C. R. Dean, *Science* **2013**, *342*, 614.
- [13] X. Hong, J. Kim, S.-F. Shi, Y. Zhang, C. Jin, Y. Sun, S. Tongay, J. Wu, Y. Zhang, F. Wang, *Nat. Nanotechnol.* **2014**, *9*, 682.
- [14] M. Sup Choi, G.-H. Lee, Y.-J. Yu, D.-Y. Lee, S. H. Lee, P. Kim, J. Hone, W. J. Yoo, *Nat. Commun.* **2013**, *4*, 1624.
- [15] M. P. Levendorf, C.-J. Kim, L. Brown, P. Y. Huang, R. W. Havener, D. A. Muller, J. Park, *Nature* **2012**, *488*, 627.
- [16] Z. Liu, L. Ma, G. Shi, W. Zhou, Y. Gong, S. Lei, X. Yang, J. Zhang, J. Yu, K. P. Hackenberg, A. Babakhani, J.-C. Idrobo, R. Vajtai, J. Lou, P. M. Ajayan, *Nat. Nanotechnol.* **2013**, *8*, 119.
- [17] L. Liu, J. Park, D. A. Siegel, K. F. McCarty, K. W. Clark, W. Deng, L. Basile, J. C. Idrobo, A.-P. Li, G. Gu, *Science* **2014**, *343*, 163.



- [18] G. H. Han, J. A. Rodríguez-Manzo, C.-W. Lee, N. J. Kybert, M. B. Lerner, Z. J. Qi, E. N. Dattoli, A. M. Rappe, M. Drndić, A. T. C. Johnson, *ACS Nano* **2013**, 7, 10129.
- [19] X. Chen, H. Yang, B. Wu, L. Wang, Q. Fu, Y. Liu, *Adv. Mater.* **2019**, 31, 1805582.
- [20] G. Iannaccone, F. Bonaccorso, L. Colombo, G. Fiori, *Nat. Nanotechnol.* **2018**, 13, 183.
- [21] G. Lu, T. Wu, P. Yang, Y. Yang, Z. Jin, W. Chen, S. Jia, H. Wang, G. Zhang, J. Sun, P. M. Ajayan, J. Lou, X. Xie, M. Jiang, *Adv. Sci.* **2017**, 4, 1700076.
- [22] Y. Gong, J. Lin, X. Wang, G. Shi, S. Lei, Z. Lin, X. Zou, G. Ye, R. Vajtai, B. I. Yakobson, H. Terrones, M. Terrones, B. K. Tay, J. Lou, S. T. Pantelides, Z. Liu, W. Zhou, P. M. Ajayan, *Nat. Mater.* **2014**, 13, 1135.
- [23] M. Shang, W. Wang, L. Zhang, S. Sun, L. Wang, L. Zhou, *J. Phys. Chem. C* **2009**, 113, 14727.
- [24] X. Wang, H. Li, H. Li, S. Lin, W. Ding, X. Zhu, Z. Sheng, H. Wang, X. Zhu, Y. Sun, *Adv. Funct. Mater.* **2020**, 30, 0190302.
- [25] Z. Xing, J. Hu, M. Ma, H. Lin, Y. An, Z. Liu, Y. Zhang, J. Li, S. Yang, *J. Am. Chem. Soc.* **2019**, 141, 19715.
- [26] J. Huang, G. Tan, H. Ren, W. Yang, C. Xu, C. Zhao, A. Xia, *ACS Appl. Mater. Interfaces* **2014**, 6, 21041.
- [27] R. He, J. Hua, A. Zhang, C. Wang, J. Peng, W. Chen, J. Zeng, *Nano Lett.* **2017**, 17, 4311.
- [28] R. Zhong, Z. Zhang, H. Yi, L. Zeng, C. Tang, L. Huang, M. Gu, *Appl. Catal., B* **2018**, 237, 1130.
- [29] Z. Zhang, P. Lin, Q. Liao, Z. Kang, H. Si, Y. Zhang, *Adv. Mater.* **2019**, 31, 1806411.
- [30] K. Chen, X. Wan, J. Xu, *Adv. Funct. Mater.* **2017**, 27, 1603884.
- [31] Y. Zhang, Y. Yao, M. G. Sendek, L. Yin, X. Zhan, F. Wang, Z. Wang, J. He, *Adv. Mater.* **2019**, 31, 1901694.
- [32] J. Shi, Q. Ji, Z. Liu, Y. Zhang, *Adv. Energy Mater.* **2016**, 6, 1600459.
- [33] J. Fu, J. Yu, C. Jiang, B. Cheng, *Adv. Energy Mater.* **2018**, 8, 1701503.
- [34] G.-C. Guo, R.-Z. Wang, B.-M. Ming, C. Wang, S.-W. Luo, M. Zhang, H. Yan, *J. Mater. Chem. A* **2019**, 7, 2106.
- [35] Q. Li, M. Liu, Y. Zhang, Z. Liu, *Small* **2016**, 12, 32.
- [36] X. Song, J. Sun, Y. Qi, T. Gao, Y. Zhang, Z. Liu, *Adv. Energy Mater.* **2016**, 6, 1600541.
- [37] Z. Kou, T. Wang, Q. Gu, M. Xiong, L. Zheng, X. Li, Z. Pan, H. Chen, F. Verpoort, A. K. Cheetham, S. Mu, J. Wang, *Adv. Energy Mater.* **2019**, 9, 1803768.
- [38] S. Thurakkal, X. Zhang, *Adv. Sci.* **2020**, 7, 1902359.
- [39] H. Liu, A. T. Neal, Z. Zhu, Z. Luo, X. Xu, D. Tománek, P. D. Ye, *ACS Nano* **2014**, 8, 4033.
- [40] W. Lei, G. Liu, J. Zhang, M. Liu, *Chem. Soc. Rev.* **2017**, 46, 3492.
- [41] R. Gusmão, Z. Sofer, M. Pumera, *Angew. Chem., Int. Ed.* **2017**, 56, 8052.
- [42] R. Gui, H. Jin, Z. Wang, J. Li, *Chem. Soc. Rev.* **2018**, 47, 6795.
- [43] B. Li, C. Lai, G. Zeng, D. Huang, L. Qin, M. Zhang, M. Cheng, X. Liu, H. Yi, C. Zhou, F. Huang, S. Liu, Y. Fu, *Small* **2019**, 15, 1804565.
- [44] Z. Hu, T. Niu, R. Guo, J. Zhang, M. Lai, J. He, L. Wang, W. Chen, *Nanoscale* **2018**, 10, 21575.
- [45] F. Xia, H. Wang, J. C. M. Hwang, A. H. C. Neto, L. Yang, *Nat. Rev. Phys.* **2019**, 1, 306.
- [46] A. Hirsch, F. Hauke, *Angew. Chem., Int. Ed.* **2018**, 57, 4338.
- [47] S. Huang, X. Ling, *Small* **2017**, 13, 1700823.
- [48] Y. Du, C. Ouyang, S. Shi, M. Lei, *J. Appl. Phys.* **2010**, 107, 093718.
- [49] N. Mao, J. Tang, L. Xie, J. Wu, B. Han, J. Lin, S. Deng, W. Ji, H. Xu, K. Liu, L. Tong, J. Zhang, *J. Am. Chem. Soc.* **2016**, 138, 300.
- [50] H. Jiang, H. Shi, X. Sun, B. Gao, *ACS Photonics* **2018**, 5, 2509.
- [51] X. Ling, S. Huang, E. H. Hasdeo, L. Liang, W. M. Parkin, Y. Tatsumi, A. R. T. Nugraha, A. A. Puzetzy, P. M. Das, B. G. Sumpter, D. B. Geohegan, J. Kong, R. Saito, M. Drndić, V. Meunier, M. S. Dresselhaus, *Nano Lett.* **2016**, 16, 2260.
- [52] R. Tian, R. Fei, S. Hu, T. Li, B. Zheng, Y. Shi, J. Zhao, L. Zhang, X. Gan, X. Wang, *Phys. Rev. B: Condens. Matter Mater. Phys.* **2020**, 101, 235407.
- [53] A. Surrente, A. A. Mitoglu, K. Galkowski, W. Tabis, D. K. Maude, P. Plochocka, *Phys. Rev. B: Condens. Matter Mater. Phys.* **2016**, 93, 121405.
- [54] M. Batmunkh, M. Bat-Erdene, J. G. Chapter, *Adv. Mater.* **2016**, 28, 8586.
- [55] H. Liu, K. Hu, D. Yan, R. Chen, Y. Zou, H. Liu, S. Wang, *Adv. Mater.* **2018**, 30, 1800295.
- [56] J. Pang, A. Bachmatiuk, Y. Yin, B. Trzebiecka, L. Zhao, L. Fu, R. G. Mendes, T. Gemming, Z. Liu, M. H. Rummeli, *Adv. Energy Mater.* **2018**, 8, 1702093.
- [57] S. Wu, K. S. Hui, K. N. Hui, *Adv. Sci.* **2018**, 5, 1700491.
- [58] H. Liu, Y. Du, Y. Deng, P. D. Ye, *Chem. Soc. Rev.* **2015**, 44, 2732.
- [59] V. Eswaraiah, Q. Zeng, Y. Long, Z. Liu, *Small* **2016**, 12, 3480.
- [60] Y. Zhang, Y. Zheng, K. Rui, H. H. Hng, K. Hippalgaonkar, J. Xu, W. Sun, J. Zhu, Q. Yan, W. Huang, *Small* **2017**, 13, 1700661.
- [61] X. Zhang, L. Hou, A. Ciesielski, P. Samorì, *Adv. Energy Mater.* **2016**, 6, 1600671.
- [62] G. Abellán, S. Wild, V. Lloret, N. Scheuschner, R. Gillen, U. Mundloch, J. Maultzsch, M. Varela, F. Hauke, A. Hirsch, *J. Am. Chem. Soc.* **2017**, 139, 10432.
- [63] T. Zhang, Y. Wan, H. Xie, Y. Mu, P. Du, D. Wang, X. Wu, H. Ji, L. Wan, *J. Am. Chem. Soc.* **2018**, 140, 7561.
- [64] A. Favron, E. Gaufres, F. Fossard, A.-L. Phaneuf-L'Heureux, N. Y. W. Tang, P. L. Lévesque, A. Loiseau, R. Leonelli, S. Francoeur, R. Martel, *Nat. Mater.* **2015**, 14, 826.
- [65] M. van Druenen, F. Davitt, T. Collins, C. Glynn, C. O'Dwyer, J. D. Holmes, G. Collins, *Langmuir* **2019**, 35, 2172.
- [66] J. Plutnar, Z. Sofer, M. Pumera, *ACS Nano* **2018**, 12, 8390.
- [67] C. R. Ryder, J. D. Wood, S. A. Wells, Y. Yang, D. Jariwala, T. J. Marks, G. C. Schatz, M. C. Hersam, *Nat. Chem.* **2016**, 8, 597.
- [68] Y. Cao, X. Tian, J. Gu, B. Liu, B. Zhang, S. Song, F. Fan, Y. Chen, *Angew. Chem., Int. Ed.* **2018**, 57, 4543.
- [69] M. van Druenen, F. Davitt, T. Collins, C. Glynn, C. O'Dwyer, J. D. Holmes, G. Collins, *Chem. Mater.* **2018**, 30, 4667.
- [70] X. Zhu, T. Zhang, Z. Sun, H. Chen, J. Guan, X. Chen, H. Ji, P. Du, S. Yang, *Adv. Mater.* **2017**, 29, 1605776.
- [71] X. Zhu, T. Zhang, D. Jiang, H. Duan, Z. Sun, M. Zhang, H. Jin, R. Guan, Y. Liu, M. Chen, H. Ji, P. Du, W. Yan, S. Wei, Y. Lu, S. Yang, *Nat. Commun.* **2018**, 9, 4177.
- [72] Z. Sofer, J. Luxa, D. Bouša, D. Sedmidubský, P. Lazar, T. Hartman, H. Hardtdegen, M. Pumera, *Angew. Chem., Int. Ed.* **2017**, 56, 9891.
- [73] J. D. Wood, S. A. Wells, D. Jariwala, K.-S. Chen, E. Cho, V. K. Sangwan, X. Liu, L. J. Lauhon, T. J. Marks, M. C. Hersam, *Nano Lett.* **2014**, 14, 6964.
- [74] J.-S. Kim, Y. Liu, W. Zhu, S. Kim, D. Wu, L. Tao, A. Dodabalapur, K. Lai, D. Akinwande, *Sci. Rep.* **2015**, 5, 8989.
- [75] P. Li, D. Zhang, J. Liu, H. Chang, Y. Sun, N. Yin, *ACS Appl. Mater. Interfaces* **2015**, 7, 24396.
- [76] Z. Yang, J. Hao, *Small Methods* **2018**, 2, 1700296.
- [77] H. Hu, H. Gao, L. Gao, F. Li, N. Xu, X. Long, Y. Hu, J. Jin, J. Ma, *Nanoscale* **2018**, 10, 5834.
- [78] Y. Wei, W.-H. Fang, R. Long, *J. Phys. Chem. Lett.* **2020**, 11, 478.
- [79] Y. Liu, P. Gao, T. Zhang, X. Zhu, M. Zhang, M. Chen, P. Du, G.-W. Wang, H. Ji, J. Yang, S. Yang, *Angew. Chem., Int. Ed.* **2019**, 58, 1479.
- [80] S. Wild, M. Fickert, A. Mitrovic, V. Lloret, C. Neiss, J. A. Vidal-Moya, M. Á. Rivero-Crespo, A. Leyva-Pérez, K. Werbach, H. Peterlik, M. Grabau, H. Wittkämper, C. Papp, H.-P. Steinrück, T. Pichler, A. Görling, F. Hauke, G. Abellán, A. Hirsch, *Angew. Chem., Int. Ed.* **2019**, 58, 5763.
- [81] L. Bai, X. Wang, S. Tang, Y. Kang, J. Wang, Y. Yu, Z.-K. Zhou, C. Ma, X. Zhang, J. Jiang, P. K. Chu, X.-F. Yu, *Adv. Mater.* **2018**, 30, 1803641.
- [82] X. Wang, Q. Li, P. Shi, J. Fan, Y. Min, Q. Xu, *Small* **2019**, 15, 1901530.

- [83] T. Wu, S. Zhang, K. Bu, W. Zhao, Q. Bi, T. Lin, J. Huang, Y. Li, F. Huang, *J. Mater. Chem. A* **2019**, 7, 22063.
- [84] J. Sun, G. Zheng, H.-W. Lee, N. Liu, H. Wang, H. Yao, W. Yang, Y. Cui, *Nano Lett.* **2014**, 14, 4573.
- [85] Y. Zhang, L. Wang, H. Xu, J. Cao, D. Chen, W. Han, *Adv. Funct. Mater.* **2020**, 30, 1909372.
- [86] X. Wu, Y. Xu, Y. Hu, G. Wu, H. Cheng, Q. Yu, K. Zhang, W. Chen, S. Chen, *Nat. Commun.* **2018**, 9, 4573.
- [87] X.-Q. Tian, X.-R. Wang, Y.-D. Wei, L. Liu, Z.-R. Gong, J. Gu, Y. Du, B. I. Yakobson, *Nano Lett.* **2017**, 17, 7995.
- [88] P. Vishnoi, K. Pramoda, U. Gupta, M. Chhetri, R. G. Balakrishna, C. N. R. Rao, *ACS Appl. Mater. Interfaces* **2019**, 11, 27780.
- [89] J. Mei, T. He, Q. Zhang, T. Liao, A. Du, G. A. Ayoko, Z. Sun, *ACS Appl. Mater. Interfaces* **2020**, 12, 21720.
- [90] T. Zhou, H. Ni, Y. Wang, C. Wu, H. Zhang, J. Zhang, A. P. Tomsia, L. Jiang, Q. Cheng, *Proc. Natl. Acad. Sci. USA* **2020**, 117, 8727.
- [91] G. Abellán, V. Lloret, U. Mundloch, M. Marcia, C. Neiss, A. Görling, M. Varela, F. Hauke, A. Hirsch, *Angew. Chem., Int. Ed.* **2016**, 55, 14557.
- [92] R. Jain, Y. Singh, S.-Y. Cho, S. P. Sasikala, S. H. Koo, R. Narayan, H.-T. Jung, Y. Jung, S. O. Kim, *Chem. Mater.* **2019**, 31, 2786.
- [93] H. Wang, K. Hu, Z. Li, C. Wang, M. Yu, Z. Li, Z. Li, *Small* **2018**, 14, 1801701.
- [94] C.-X. Hu, Q. Xiao, Y.-Y. Ren, M. Zhao, G.-H. Dun, H.-R. Wu, X.-Y. Li, Q.-Q. Yang, B. Sun, Y. Peng, F. Yan, Q. Wang, H.-L. Zhang, *Adv. Funct. Mater.* **2018**, 28, 1805311.
- [95] R. Gusmão, Z. Sofer, M. Pumera, *ACS Nano* **2018**, 12, 5666.
- [96] S. Zhao, J. Wu, K. Jin, H. Ding, T. Li, C. Wu, N. Pan, X. Wang, *Adv. Funct. Mater.* **2018**, 28, 1802011.
- [97] J. Bullock, M. Amani, J. Cho, Y.-Z. Chen, G. H. Ahn, V. Adinolfi, V. R. Shrestha, Y. Gao, K. B. Crozier, Y.-L. Chueh, A. Javey, *Nat. Photonics* **2018**, 12, 601.
- [98] R. A. Doganov, E. C. T. O'Farrell, S. P. Koenig, Y. Yeo, A. Ziletti, A. Carvalho, D. K. Campbell, D. F. Coker, K. Watanabe, T. Taniguchi, A. H. C. Neto, B. Özyilmaz, *Nat. Commun.* **2015**, 6, 6647.
- [99] L. Ye, P. Wang, W. Luo, F. Gong, L. Liao, T. Liu, L. Tong, J. Zang, J. Xu, W. Hu, *Nano Energy* **2017**, 37, 53.
- [100] D. Li, B. Wang, M. Chen, J. Zhou, Z. Zhang, *Small* **2017**, 13, 1603726.
- [101] D. Li, X. Wang, Q. Zhang, L. Zou, X. Xu, Z. Zhang, *Adv. Funct. Mater.* **2015**, 25, 7360.
- [102] X. Chen, Y. Wu, Z. Wu, Y. Han, S. Xu, L. Wang, W. Ye, T. Han, Y. He, Y. Cai, N. Wang, *Nat. Commun.* **2015**, 6, 7315.
- [103] A. Gao, J. Lai, Y. Wang, Z. Zhu, J. Zeng, G. Yu, N. Wang, W. Chen, T. Cao, W. Hu, D. Sun, X. Chen, F. Miao, Y. Shi, X. Wang, *Nat. Nanotechnol.* **2019**, 14, 217.
- [104] Z. Wang, L. Chu, L. Li, M. Yang, J. Wang, G. Eda, K. P. Loh, *Nano Lett.* **2019**, 19, 2840.
- [105] K. Chaudhary, M. Tamagnone, M. Rezaee, D. K. Bediako, A. Ambrosio, P. Kim, F. Capasso, *Sci. Adv.* **2019**, 5, eaau7171.
- [106] X. Xiong, M. Huang, B. Hu, X. Li, F. Liu, S. Li, M. Tian, T. Li, J. Song, Y. Wu, *Nat. Electron.* **2020**, 3, 106.
- [107] M. A. Huber, F. Mooshammer, M. Plankl, L. Viti, F. Sandner, L. Z. Kastner, T. Frank, J. Fabian, M. S. Vitiello, T. L. Cocker, R. Huber, *Nat. Nanotechnol.* **2017**, 12, 207.
- [108] M. Huang, S. Li, Z. Zhang, X. Xiong, X. Li, Y. Wu, *Nat. Nanotechnol.* **2017**, 12, 1148.
- [109] Y. Deng, Z. Luo, N. J. Conrad, H. Liu, Y. Gong, S. Najmaei, P. M. Ajayan, J. Lou, X. Xu, P. D. Ye, *ACS Nano* **2014**, 8, 8292.
- [110] J. Mei, Y. Zhang, T. Liao, X. Peng, G. A. Ayoko, Z. Sun, *Energy Storage Mater.* **2019**, 19, 424.
- [111] Y. Liu, J. N. B. Rodrigues, Y. Z. Luo, L. Li, A. Carvalho, M. Yang, E. Laksono, J. Lu, Y. Bao, H. Xu, S. J. R. Tan, Z. Qiu, C. H. Sow, Y. P. Feng, A. H. C. Neto, S. Adam, J. Lu, K. P. Loh, *Nat. Nanotechnol.* **2018**, 13, 828.
- [112] M. Zhu, Z. Sun, M. Fujitsuka, T. Majima, *Angew. Chem., Int. Ed.* **2018**, 57, 2160.
- [113] Q. Zhang, S. Huang, J. Deng, D. T. Gangadharan, F. Yang, Z. Xu, G. Giorgi, M. Palummo, M. Chaker, D. Ma, *Adv. Funct. Mater.* **2019**, 29, 1902486.
- [114] R. Zhao, Z. Qian, Z. Liu, D. Zhao, X. Hui, G. Jiang, C. Wang, L. Yin, *Nano Energy* **2019**, 65, 104037.
- [115] J. M. Urban, M. Baranowski, A. Surrente, D. Włodarczyk, A. Suchocki, G. Long, Y. Wang, L. Kłopotowski, N. Wang, D. K. Maude, P. Plochocka, *Nanoscale* **2017**, 9, 19298.
- [116] M. Birowska, J. Urban, M. Baranowski, D. K. Maude, P. Plochocka, N. G. Szwacki, *Nanotechnology* **2019**, 30, 195201.
- [117] F. Xia, H. Wang, Y. Jia, *Nat. Commun.* **2014**, 5, 4458.
- [118] X. Wang, A. M. Jones, K. L. Seyler, V. Tran, Y. Jia, H. Zhao, H. Wang, L. Yang, X. Xu, F. Xia, *Nat. Nanotechnol.* **2015**, 10, 517.
- [119] Y. Yi, Z. Sun, J. Li, P. K. Chu, X.-F. Yu, *Small Methods* **2019**, 3, 1900165.
- [120] L. Li, Y. Yu, G. J. Ye, Q. Ge, X. Ou, H. Wu, D. Feng, X. H. Chen, Y. Zhang, *Nat. Nanotechnol.* **2014**, 9, 372.
- [121] J. Yuan, S. Najmaei, Z. Zhang, J. Zhang, S. Lei, P. M. Ajayan, B. I. Yakobson, J. Lou, *ACS Nano* **2015**, 9, 555.
- [122] L. Huang, N. Huo, Y. Li, H. Chen, J. Yang, Z. Wei, J. Li, S.-S. Li, *J. Phys. Chem. Lett.* **2015**, 6, 2483.
- [123] Y. Cai, G. Zhang, Y.-W. Zhang, *J. Phys. Chem. C* **2015**, 119, 13929.
- [124] W. Hu, T. Wang, J. Yang, *J. Mater. Chem. C* **2015**, 3, 4756.
- [125] G. C. Constantinescu, N. D. M. Hine, *Nano Lett.* **2016**, 16, 2586.
- [126] N. Gillgren, D. Wickramaratne, Y. Shi, T. Espiritu, J. Yang, J. Hu, J. Wei, X. Liu, Z. Mao, K. Watanabe, T. Taniguchi, M. Bockrath, Y. Barlas, R. K. Lake, C. N. Lau, *2D Mater.* **2014**, 2, 011001.
- [127] K. Tran, G. Moody, F. Wu, X. Lu, J. Choi, K. Kim, A. Rai, D. A. Sanchez, J. Quan, A. Singh, J. Embley, A. Zepeda, M. Campbell, T. Autry, T. Taniguchi, K. Watanabe, N. Lu, S. K. Banerjee, K. L. Silverman, S. Kim, E. Tutuc, L. Yang, A. H. MacDonald, X. Li, *Nature* **2019**, 567, 71.
- [128] Y. Cao, V. Fatemi, S. Fang, K. Watanabe, T. Taniguchi, E. Kaxiras, P. Jarillo-Herrero, *Nature* **2018**, 556, 43.
- [129] S. Brem, K.-Q. Lin, R. Gillen, J. M. Bauer, J. Maultzsch, J. M. Lupton, E. Malic, *Nanoscale* **2020**, 12, 11088.
- [130] P. Kang, W.-T. Zhang, V. Michaud-Rioux, X.-H. Kong, C. Hu, G.-H. Yu, H. Guo, *Phys. Rev. B: Condens. Matter Mater. Phys.* **2017**, 96, 195406.
- [131] G. Long, D. Maryenko, J. Shen, S. Xu, J. Hou, Z. Wu, W. K. Wong, T. Han, J. Lin, Y. Cai, R. Lortz, N. Wang, *Nano Lett.* **2016**, 16, 7768.
- [132] J. Kang, D. Jariwala, C. R. Ryder, S. A. Wells, Y. Choi, E. Hwang, J. H. Cho, T. J. Marks, M. C. Hersam, *Nano Lett.* **2016**, 16, 2580.
- [133] S. Kim, G. Myeong, J. Park, K. Watanabe, T. Taniguchi, S. Cho, *Nano Lett.* **2020**, 20, 3963.
- [134] J. Bi, X. Zou, Y. Lv, G. Li, X. Liu, Y. Liu, T. Yu, Z. Yang, L. Liao, *Adv. Electron. Mater.* **2020**, 6, 2000291.
- [135] K. Xu, E. Wynne, W. Zhu, *Adv. Electron. Mater.* **2020**, 6, 2000318.
- [136] A. Gao, Z. Zhang, L. Li, B. Zheng, C. Wang, Y. Wang, T. Cao, Y. Wang, S.-J. Liang, F. Miao, Y. Shi, X. Wang, *ACS Nano* **2020**, 14, 434.
- [137] L. Li, F. Yang, G. J. Ye, Z. Zhang, Z. Zhu, W. Lou, X. Zhou, L. Li, K. Watanabe, T. Taniguchi, K. Chang, Y. Wang, X. H. Chen, Y. Zhang, *Nat. Nanotechnol.* **2016**, 11, 593.
- [138] A. Avsar, I. J. Vera-Marun, J. Y. Tan, K. Watanabe, T. Taniguchi, A. H. Castro Neto, B. Özyilmaz, *ACS Nano* **2015**, 9, 4138.
- [139] D.-K. Kim, S.-B. Hong, K. Jeong, C. Lee, H. Kim, M.-H. Cho, *ACS Nano* **2019**, 13, 1683.
- [140] X. Liu, D. Qu, H.-M. Li, I. Moon, F. Ahmed, C. Kim, M. Lee, Y. Choi, J. H. Cho, J. C. Hone, W. J. Yoo, *ACS Nano* **2017**, 11, 9143.
- [141] Q. Lv, F. Yan, N. Mori, W. Zhu, C. Hu, Z. R. Kudrynskiy, Z. D. Kovalyuk, A. Patané, K. Wang, *Adv. Funct. Mater.* **2020**, 30, 1910713.

- [142] Y. Hassan, P. K. Srivastava, B. Singh, M. S. Abbas, F. Ali, W. J. Yoo, C. Lee, *ACS Appl. Mater. Interfaces* **2020**, 12, 14119.
- [143] S. Yan, H. Huang, Z. Xie, G. Ye, X.-X. Li, T. Taniguchi, K. Watanabe, Z. Han, X. Chen, J. Wang, J.-H. Chen, *ACS Appl. Mater. Interfaces* **2019**, 11, 42358.
- [144] J. Na, Y. Kim, J. H. Smet, M. Burghard, K. Kern, *ACS Appl. Mater. Interfaces* **2019**, 11, 20973.
- [145] N. Youngblood, C. Chen, S. J. Koester, M. Li, *Nat. Photonics* **2015**, 9, 247.
- [146] Y. Liu, B. N. Shivananju, Y. Wang, Y. Zhang, W. Yu, S. Xiao, T. Sun, W. Ma, H. Mu, S. Lin, H. Zhang, Y. Lu, C.-W. Qiu, S. Li, Q. Bao, *ACS Appl. Mater. Interfaces* **2017**, 9, 36137.
- [147] L. Ye, H. Li, Z. Chen, J. Xu, *ACS Photonics* **2016**, 3, 692.
- [148] L. Wang, X. Zou, J. Lin, J. Jiang, Y. Liu, X. Liu, X. Zhao, Y. F. Liu, J. C. Ho, L. Liao, *ACS Nano* **2019**, 13, 4804.
- [149] A. M. Afzal, G. Dastgeer, M. Z. Iqbal, P. Gautam, M. M. Faisal, *ACS Appl. Mater. Interfaces* **2020**, 12, 19625.
- [150] M. Donarelli, L. Ottaviano, *Sensors* **2018**, 18, 3638.
- [151] M. Feierabend, G. Berghäuser, A. Knorr, E. Malic, *Nat. Commun.* **2017**, 8, 14776.
- [152] Y. Cai, Q. Ke, G. Zhang, Y.-W. Zhang, *J. Phys. Chem. C* **2015**, 119, 3102.
- [153] M. Donarelli, L. Ottaviano, L. Giancaterini, G. Fioravanti, F. Perrozzi, C. Cantalini, *2D Mater.* **2016**, 3, 025002.
- [154] A. N. Abbas, B. Liu, L. Chen, Y. Ma, S. Cong, N. Aroonyadet, M. Köpf, T. Nilges, C. Zhou, *ACS Nano* **2015**, 9, 5618.
- [155] Z. Feng, B. Chen, S. Qian, L. Xu, L. Feng, Y. Yu, R. Zhang, J. Chen, Q. Li, Q. Li, C. Sun, H. Zhang, J. Liu, W. Pang, D. Zhang, *2D Mater.* **2016**, 3, 035021.
- [156] J. Sun, H.-W. Lee, M. Pasta, H. Yuan, G. Zheng, Y. Sun, Y. Li, Y. Cui, *Nat. Nanotechnol.* **2015**, 10, 980.
- [157] S. Shi, R. Hu, E. Wu, Q. Li, X. Chen, W. Guo, C. Sun, X. Hu, D. Zhang, J. Liu, *Nanotechnology* **2018**, 29, 435502.
- [158] J.-S. Jang, H. J. Jung, S. Chong, D.-H. Kim, J. Kim, S. O. Kim, I.-D. Kim, *Adv. Mater.* **2020**, 32, 2002723.
- [159] C.-M. Park, H.-J. Sohn, *Adv. Mater.* **2007**, 19, 2465.
- [160] L. Li, L. Chen, S. Mukherjee, J. Gao, H. Sun, Z. Liu, X. Ma, T. Gupta, C. V. Singh, W. Ren, H.-M. Cheng, N. Koratkar, *Adv. Mater.* **2017**, 29, 1602734.
- [161] X. Guo, W. Zhang, J. Zhang, D. Zhou, X. Tang, X. Xu, B. Li, H. Liu, G. Wang, *ACS Nano* **2020**, 14, 3651.
- [162] X. Wu, H. Wang, Z. Zhao, B. Huang, *J. Mater. Chem. A* **2020**, 8, 12705.
- [163] B. Yang, C. Hao, F. Wen, B. Wang, C. Mu, J. Xiang, L. Li, B. Xu, Z. Zhao, Z. Liu, Y. Tian, *ACS Appl. Mater. Interfaces* **2017**, 9, 44478.
- [164] L. Chen, G. Zhou, Z. Liu, X. Ma, J. Chen, Z. Zhang, X. Ma, F. Li, H.-M. Cheng, W. Ren, *Adv. Mater.* **2016**, 28, 510.
- [165] M. Li, N. Muralidharan, K. Moyer, C. L. Pint, *Nanoscale* **2018**, 10, 10443.
- [166] F. Wang, X. Wu, X. Yuan, Z. Liu, Y. Zhang, L. Fu, Y. Zhu, Q. Zhou, Y. Wu, W. Huang, *Chem. Soc. Rev.* **2017**, 46, 6816.
- [167] T. Lv, M. Liu, D. Zhu, L. Gan, T. Chen, *Adv. Mater.* **2018**, 30, 1705489.
- [168] X. Chen, G. Xu, X. Ren, Z. Li, X. Qi, K. Huang, H. Zhang, Z. Huang, J. Zhong, *J. Mater. Chem. A* **2017**, 5, 6581.
- [169] P. Vishnoi, U. Gupta, R. Pandey, C. N. R. Rao, *J. Mater. Chem. A* **2019**, 7, 6631.
- [170] X. Chen, S. Shen, L. Guo, S. S. Mao, *Chem. Rev.* **2010**, 110, 6503.
- [171] A. Fujishima, K. Honda, *Nature* **1972**, 238, 37.
- [172] M. Z. Rahman, M. G. Kibria, C. B. Mullins, *Chem. Soc. Rev.* **2020**, 49, 1887.
- [173] M. Zhu, S. Kim, L. Mao, M. Fujitsuka, J. Zhang, X. Wang, T. Majima, *J. Am. Chem. Soc.* **2017**, 139, 13234.
- [174] J. Ran, W. Guo, H. Wang, B. Zhu, J. Yu, S.-Z. Qiao, *Adv. Mater.* **2018**, 30, 1800128.
- [175] J. Hu, D. Chen, Z. Mo, N. Li, Q. Xu, H. Li, J. He, H. Xu, J. Lu, *Angew. Chem., Int. Ed.* **2019**, 58, 2073.
- [176] Y. Zheng, Y. Chen, B. Gao, B. Lin, X. Wang, *Adv. Funct. Mater.* **2020**, 30, 2002021.
- [177] B. Shao, J. Wang, Z. Liu, G. Zeng, L. Tang, Q. Liang, Q. He, T. Wu, Y. Liu, X. Yuan, *J. Mater. Chem. A* **2020**, 8, 5171.
- [178] Y. Zheng, Z. Yu, H. Ou, A. M. Asiri, Y. Chen, X. Wang, *Adv. Funct. Mater.* **2018**, 28, 1705407.
- [179] M. Vanni, M. Serrano-Ruiz, F. Telesio, S. Heun, M. Banchelli, P. Matteini, A. M. Mio, G. Nicotra, C. Spinella, S. Caporali, A. Giaccherini, F. D'Acapito, M. Caporali, M. Peruzzini, *Chem. Mater.* **2019**, 31, 5075.
- [180] K. Ge, Y. Zhang, D. Wang, Z. Li, J. He, C. Fu, Y. Yang, M. Pan, L. Zhu, *ACS Appl. Mater. Interfaces* **2020**, 12, 20035.
- [181] J. Hu, Y. Ji, Z. Mo, N. Li, Q. Xu, Y. Li, H. Xu, D. Chen, J. Lu, *J. Mater. Chem. A* **2019**, 7, 4408.
- [182] Y. Chen, T. Shi, P. Liu, X. Ma, L. Shui, C. Shang, Z. Chen, X. Wang, K. Kempa, G. Zhou, *J. Mater. Chem. A* **2018**, 6, 19167.
- [183] J. Wang, D. Liu, H. Huang, N. Yang, B. Yu, M. Wen, X. Wang, P. K. Chu, X.-F. Yu, *Angew. Chem., Int. Ed.* **2018**, 57, 2600.
- [184] Y. Li, Y. Sun, Y. Qin, W. Zhang, L. Wang, M. Luo, H. Yang, S. Guo, *Adv. Energy Mater.* **2020**, 10, 1903120.
- [185] J. Hou, Y. Wu, B. Zhang, S. Cao, Z. Li, L. Sun, *Adv. Funct. Mater.* **2019**, 29, 1808367.
- [186] T. Reier, M. Oezaslan, P. Strasser, *ACS Catal.* **2012**, 2, 1765.
- [187] G. C. da Silva, M. R. Fernandes, E. A. Ticianelli, *ACS Catal.* **2018**, 8, 10096.
- [188] J. Yu, Y. Guo, S. She, S. Miao, M. Ni, W. Zhou, M. Liu, Z. Shao, *Adv. Mater.* **2018**, 30, 1800047.
- [189] Z. Yuan, J. Li, M. Yang, Z. Fang, J. Jian, D. Yu, X. Chen, L. Dai, *J. Am. Chem. Soc.* **2019**, 141, 4972.
- [190] T. Wu, Y. Ma, Z. Qu, J. Fan, Q. Li, P. Shi, Q. Xu, Y. Min, *ACS Appl. Mater. Interfaces* **2019**, 11, 5136.
- [191] T. F. Jaramillo, K. P. Jørgensen, J. Bonde, J. H. Nielsen, S. Hørch, I. Chorkendorff, *Science* **2007**, 317, 100.
- [192] B. Hinnemann, P. G. Moses, J. Bonde, K. P. Jørgensen, J. H. Nielsen, S. Hørch, I. Chorkendorff, J. K. Nørskov, *J. Am. Chem. Soc.* **2005**, 127, 5308.
- [193] T. Wu, J. Fan, Q. Li, P. Shi, Q. Xu, Y. Min, *Adv. Energy Mater.* **2018**, 8, 1701799.
- [194] H. Huang, L. He, W. Zhou, G. Qu, J. Wang, N. Yang, J. Gao, T. Chen, P. K. Chu, X.-F. Yu, *Biomaterials* **2018**, 171, 12.
- [195] B. Yang, J. Yin, Y. Chen, S. Pan, H. Yao, Y. Gao, J. Shi, *Adv. Mater.* **2018**, 30, 1705611.
- [196] G. Qu, W. Liu, Y. Zhao, J. Gao, T. Xia, J. Shi, L. Hu, W. Zhou, J. Gao, H. Wang, Q. Luo, Q. Zhou, S. Liu, X.-F. Yu, G. Jiang, *Angew. Chem., Int. Ed.* **2017**, 56, 14488.
- [197] Y. Zhao, L. Tong, Z. Li, N. Yang, H. Fu, L. Wu, H. Cui, W. Zhou, J. Wang, H. Wang, P. K. Chu, X.-F. Yu, *Chem. Mater.* **2017**, 29, 7131.
- [198] H. Wang, X. Yang, W. Shao, S. Chen, J. Xie, X. Zhang, J. Wang, Y. Xie, *J. Am. Chem. Soc.* **2015**, 137, 11376.
- [199] W. Chen, J. Ouyang, X. Yi, Y. Xu, C. Niu, W. Zhang, L. Wang, J. Sheng, L. Deng, Y.-N. Liu, S. Guo, *Adv. Mater.* **2018**, 30, 1703458.
- [200] J. Shao, H. Xie, H. Huang, Z. Li, Z. Sun, Y. Xu, Q. Xiao, X.-F. Yu, Y. Zhao, H. Zhang, H. Wang, P. K. Chu, *Nat. Commun.* **2016**, 7, 12967.
- [201] M. Luo, T. Fan, Y. Zhou, H. Zhang, L. Mei, *Adv. Funct. Mater.* **2019**, 29, 1808306.
- [202] X. Ge, Z. Xia, S. Guo, *Adv. Funct. Mater.* **2019**, 29, 1900318.
- [203] C. Xu, Y. Xu, M. Yang, Y. Chang, A. Nie, Z. Liu, J. Wang, Z. Luo, *Adv. Funct. Mater.* **2020**, 30, 2000177.
- [204] M. Zhang, Z. Cui, R. Song, B. Lv, Z. Tang, X. Meng, X. Chen, X. Zheng, J. Zhang, Z. Yao, W. Bu, *Biomaterials* **2018**, 155, 135.
- [205] A. Kamkaew, F. Chen, Y. Zhan, R. L. Majewski, W. Cai, *ACS Nano* **2016**, 10, 3918.

- [206] Z. Guo, S. Zhu, Y. Yong, X. Zhang, X. Dong, J. Du, J. Xie, Q. Wang, Z. Gu, Y. Zhao, *Adv. Mater.* **2017**, 29, 1704136.
- [207] G. Tian, X. Zhang, Z. Gu, Y. Zhao, *Adv. Mater.* **2015**, 27, 7692.
- [208] X. Liu, A. L. Miller, S. Park, M. N. George, B. E. Waletzki, H. Xu, A. Terzic, L. Lu, *ACS Appl. Mater. Interfaces* **2019**, 11, 23558.
- [209] M. Bolognesi, M. Brucale, A. Lorenzoni, F. Prescimone, S. Moschetto, V. V. Korolkov, M. Baldoni, M. Serrano-Ruiz, M. Caporali, F. Mercuri, E. Besley, M. Muccini, M. Peruzzini, P. H. Beton, S. Toffanin, *Nanoscale* **2019**, 11, 17252.
- [210] B. Lu, X. Zheng, Z. Li, *Nanoscale* **2020**, 12, 6617.
- [211] R. Perea-Causín, S. Brem, R. Rosati, R. Jago, M. Kulig, J. D. Ziegler, J. Zipfel, A. Chernikov, E. Malic, *Nano Lett.* **2019**, 19, 7317.
- [212] Z. Cai, B. Liu, X. Zou, H.-M. Cheng, *Chem. Rev.* **2018**, 118, 6091.
- [213] J. Wang, A. Rousseau, M. Yang, T. Low, S. Francoeur, S. Kéna-Cohen, *Nano Lett.* **2020**, 20, 3651.
- [214] X. Zong, H. Hu, G. Ouyang, J. Wang, R. Shi, L. Zhang, Q. Zeng, C. Zhu, S. Chen, C. Cheng, B. Wang, H. Zhang, Z. Liu, W. Huang, T. Wang, L. Wang, X. Chen, *Light: Sci. Appl.* **2020**, 9, 114.



**Shameel Thurakkal** is a postdoctoral fellow in Prof. Xiaoyan Zhang's group at the Department of Chemistry and Chemical Engineering, Chalmers University of Technology, Sweden. He received his Ph.D. degree from CSIR-National Institute for Interdisciplinary Science and Technology in 2018. His current research interest is chemical functionalization of 2D materials for applications in energy storage and catalysis.



**Xiaoyan Zhang** is working as an assistant professor at the Department of Chemistry and Chemical Engineering, Chalmers University of Technology, Sweden. He received his Ph.D. degree from the University of Groningen, the Netherlands, followed by postdoctoral research at the University of Strasbourg, France. His research team at Chalmers is currently focusing on chemical functionalization of 2D materials for ad-hoc applications.